Nano-Materials and Electronic Devices

Academic and Research Staff
Professor Jing Kong

Visiting Scientists and Research Affiliates
Kikang Kim, Sreekar Bhaviripudi

Visiting Students
Yaping Hsieh, Yumeng Shi

Graduate Students
Hootan Farhat, Mario Hofmann, Daniel Nezich, Alfonso R. Reina Cecco, KyeongJae Lee, Allen Hsu, Hyesung Park

Technical and Support Staff
Evan Moran

The RLE Nano-materials and Electronics Group pursues investigations of carbon nanotubes, including studies of chemical vapor deposition methods, electron transport in single-walled carbon nanotubes, nanotube synthesis, and tunable Raman systems for characterizing the chirality of nanotube materials. A major objective of the group is to develop synthesis and control techniques to create electronic devices based on carbon nanotubes.

1. Large Area, Few-Layer Graphene Films on Arbitrary Substrates by Chemical Vapor Deposition

Sponsors
Support of the Lincoln Lab Advanced Concept committee for the initiation of the work and Intel Higher Education Program. This work was partly supported under NSF grant NIRT CTS-05-06830 (X. J. and M. S. D) and NSF DMR 07-04197 (A.R. and M.S.D) and by a Xerox fellowship (H. S). Raman measurements were carried out in the George R. Harrison Spectroscopy Laboratory supported by NSF-CHE 0111370 and NIH-RR02594 grants.

Project Staff
Alfonso Reina, Xiaoting Jia, John Ho, Daniel Nezich, Hyungbin Son, Vladimir Bulovic, Mildred S. Dresselhaus and Jing Kong

Graphene is the hexagonal arrangement of carbon atoms forming a one-atom thick planar sheet. The successful isolation of graphene by the micro-cleaving of highly oriented pyrolytic graphite (HOPG)[1] has opened up exciting possibilities for experimental investigations[2, 3]. Significant attention has been captured by its outstanding properties which render it another materials option for electronics applications[4-9]. Chemical routes to fabricate graphene may offer significant advantages over the micro-cleaving of HOPG [10-14] when pursuing the coverage of large substrate areas with graphene for large scale applications. Methods for large area graphene synthesis include ultra-high vacuum (UHV) annealing of single-crystal SiC (0001) [13, 15], UHV CVD on single crystal transition metals[12] and the deposition of graphene oxide (GO) films from a liquid suspension followed by chemical reduction [10, 16]. However, some of these approaches require the use of a specific substrate material. Furthermore, the high cost of the single crystal substrates and the UHV conditions necessary for growth significantly limit the use of these methods for large scale applications. Films derived from liquid suspensions of graphene flakes can potentially overcome these limitations [10, 17-19]. However, in this case, the intrinsic properties of graphene have not yet been achieved[10, 17-19]. In the present work, we use ambient-pressure CVD to synthesize single- to few layer graphene films on evaporated polycrystalline Ni. Due to the use of ambient pressure and readily available Ni films, this process enables the inexpensive and high-throughput growth of graphene over large areas with properties closer to those found by micro-cleaving HOPG. Additionally, our method allows the flexibility of transferring the produced film to alternative substrates by wet-etching the Ni film. The graphene films can then be used without further treatment and exhibit outstanding properties in terms of optical transparency and electrical conductivity. In principle, there is no limitation on the film size, and it can be patterned by standard lithographic processes. Alternatively, the catalytic Ni

surface can be pre-patterned in order to produce graphene patterns of desired geometries at controlled locations.

The growth of graphene monolayers on single crystalline transition metals such as Co[20], Pt[21, 22], Ir[23, 24], Ru[25, 26] and Ni[27-31] is well known. The nucleation and growth of graphene usually occurs by exposure of the transition metal surface to a hydrocarbon gas under low pressure or UHV conditions. In our CVD process, we expose a polycrystalline Ni film (at 900-1000 ˚C) to a highly diluted hydrocarbon flow under ambient pressure (see Supporting Information). This gives rise to an ultra thin graphene film (1 to ~10 layers) over the Ni surface. The Ni film is e-beam evaporated onto a SiO_2/Si substrates, and thermally annealed before the CVD synthesis. Thermal annealing before the CVD process generates a Ni film microstructure with single-crystalline grains of sizes between a few μm to 20 μm. The surfaces of these grains have atomically flat terraces and steps, similarly to the surface of single crystal substrates used for epitaxial UHV graphene growth [12, 13] (Fig. 1a). In this way, the growth of graphene on the surface of individual Ni grains resembles the growth of graphene on the surface of a single crystal substrate. In our CVD process, graphene growth is likely to occur due to the precipitation of graphite from carbon species within the Ni film as observed for other transition metals, such as Ru.[12] During the exposure of the Ni surface to a H_2 and CH_4 gas mixture in atmospheric conditions, the Ni film and the carbon atoms provided by this CVD process form a solid solution. Since the solubility of carbon in Ni is temperature-dependent, carbon atoms precipitate as a graphene layer on the Ni surface upon cooling of the sample. Due to the formation of grain boundaries, the top surface of the Ni film becomes discontinuous after the thermal annealing. Nevertheless, we found that single- and few-layer graphene bridges across these gaps, thus forming a continuous film over the entire Ni area (Fig. 1b).

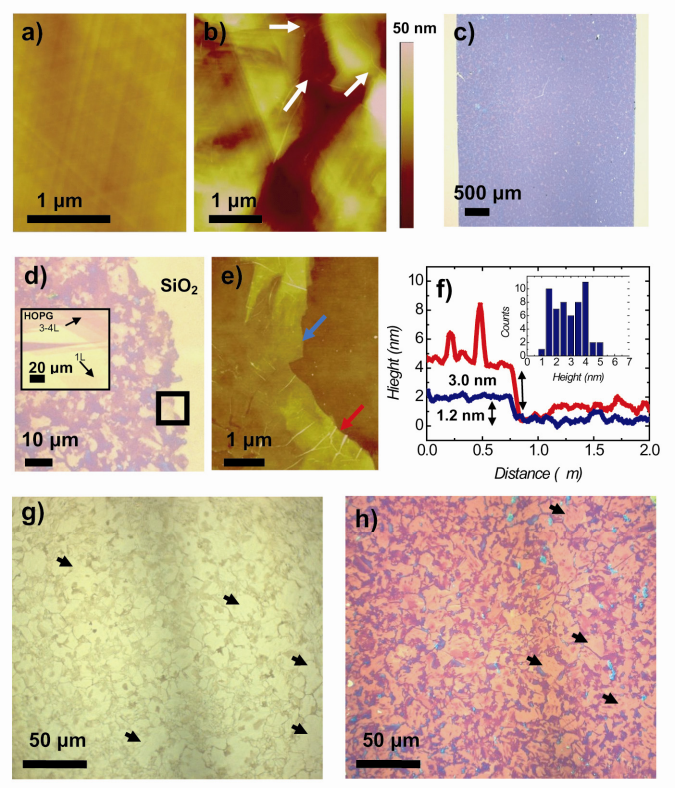

Figure 1. Graphene films grown by CVD on Ni. **a,** AFM image of the surface of a Ni grain with atomically flat terraces and steps after annealing. **b,** AFM image of a graphene film on polycrystalline Ni after CVD synthesis. The ripples (pointed out by white arrows) at the edge of the groove indicate that the film growth bridges across the gaps between grains. **c,** Optical image of a CVD-grown graphene film (blue) transferred to a SiO_2/Si substrate (yellow background). The size of the graphene film is determined by the size of the initial Ni substrate. **d**, Optical image of an edge of a graphene film on a SiO_2/Si substrate. Graphene on SiO_2/Si obtained by HOPG cleaving is shown in the inset for comparison. **e,** AFM image of the region enclosed by the black square in (d). The blue (red) arrow corresponds to the pink (purple) region in (d). **f**, Height measurements on the two positions indicated in (e). The blue (red) curve corresponds to the region identified by the blue (red) arrow in (e). The height distribution, measured by AFM images taken from the film edge in (d), is shown as an inset. **g,** Optical image of a Ni film after the CVD process and with a graphene film on its surface. **h,** Optical image of the same graphene film in (g) transferred to a SiO_2/Si substrate showing a high density of large regions (1-20 μm) consisting of 1-2 layers of graphene (identified by the black arrows). These regions grow on the large Ni grains, identified by the arrows in (g). The morphology (shape and size) of graphene regions with constant thickness resemble the morphology of the Ni grains in (g). Color scale bar corresponds to (a,b).

The transfer of the CVD-derived graphene films to a non-specific substrate is enabled by the wet-etching of the underlying Ni film. This is carried out by treating the film with an aqueous HCl solution after a support material is coated on the Ni/graphene surface, in our case a poly[methyl methacrylate] (PMMA) layer (see Supporting Information). This results in a free standing PMMA/graphene membrane which can be handled easily and placed on the desired target substrate (graphene facing the surface)[32]. Finally, the PMMA can be dissolved with acetone to yield a graphene film on the desired substrate. The transferred graphene films preserve their continuity and attach strongly to substrates made of almost any material, such as semiconductors, glass, metals and plastics, via van der Waals interactions. In the case of SiO_2/Si substrates, the attached graphene films can successfully withstand harsh processing procedures, such as

sonication or acidic treatment. The size and shape of the transferred graphene film on the new substrate is defined by the dimensions of the initial Ni-coated substrate (Fig. 1c).

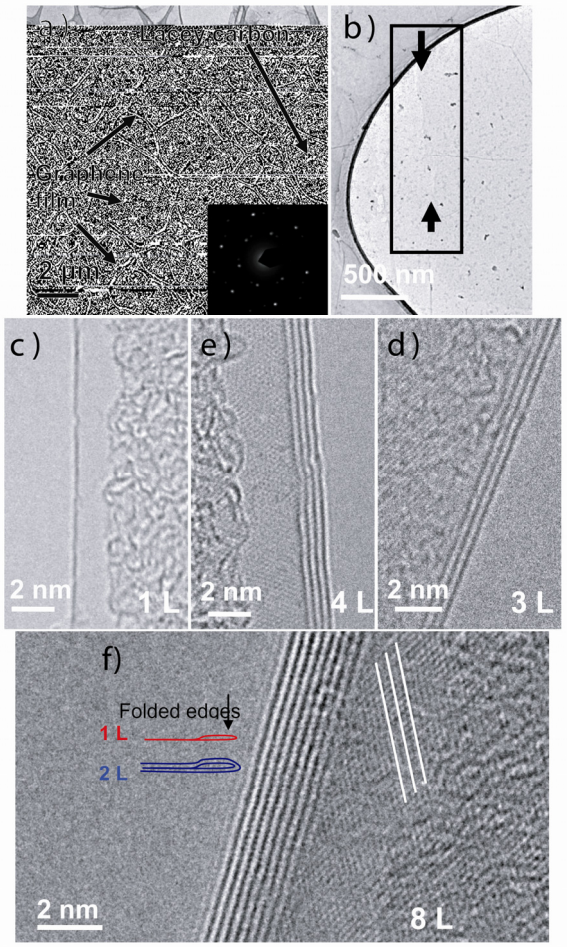

Figure 2. TEM characterization of CVD-grown graphene films. **a,** Low magnification TEM image showing a CVD-grown graphene film on a lacey carbon coated grid. Electron diffraction on the graphene film is shown as an inset. **b**, Low magnification TEM image showing the interface between areas with different thickness (identified by the black arrow). Although the color contrast is high under optical images, the low contrast in TEM images shows that the thickness difference is only a few graphene layers. **c-f**, High magnification TEM images showing the edges of film regions consisting of one (c), three (d), four (e), and eight (f) graphene layers. The cross-sectional view is enabled by the folding of the film edge. The in-plane lattice fringes suggest local stacking order of the graphene layers.

Important morphological film features are revealed by optical images when the films are on Si substrates with a 300 nm oxide layer (Fig. 1d). Variations in the film thickness are indicated by the change of color contrast in the optical images, due to light interference on the SiO_2 layer modulated by the graphene layers[33, 34]. The differences in thickness range from a monolayer to a few graphene layers. The lightest pink regions in the optical images (Fig. 1d) have a thickness of roughly 1 nm, as measured by AFM (Fig. 1e-f), which typically corresponds to a monolayer or bilayer of graphene [35, 36]. Purple regions correspond to 3.0 nm thickness. Height measurements extracted from a series of AFM images along the film edge in Fig. 1d shows that the thickness ranges from 1 to 5 nm (inset of Fig. 1f, with an average of 2.8nm ± 0.3), corresponding to approximately 1-12 graphene layers [35]. Furthermore, the mean and the RMS roughness estimated with our AFM data are 1.97 nm and 3.27 nm, respectively, over a 100 μm^2 area (see Supporting Information). By comparing optical images of as-grown graphene films on the Ni surface and their images after being transferred to SiO_2/Si (Fig. 1g and 1h), we observe that the morphologies of the graphene film correlate qualitatively with the microstructure of the Ni films. For example, we observe a high density of regions with only 1-2 graphene layers in thickness and 1μm- 20 μm in lateral dimensions (black arrows in Fig. 1h). Further analysis (see Supporting Information) confirms that these regions usually grow on the surface of large Ni grains which have similar lateral sizes (black arrows in Fig. 1g). These observations imply that individual nickel grains may independently affect the thickness of the graphene film during CVD, leading to the thickness variations we observe on our films. Similarly, our observations suggest that most of the multilayer graphene nucleation occurs at the grain boundaries. This could be explained by the fact that at such boundaries, there is a higher density of atomic steps due to the curvature of the grain edge, thereby inducing the nucleation of several graphene layers[12]. This points to future work controlling the morphology of the Ni films in order to optimize the morphology of the graphene films.

The CVD grown films can be transferred by the same method to TEM lacey carbon coated grids (Fig. 2a-b). TEM examination confirms that changes in film thickness correspond to only a few graphene layers. The edges of the suspended film always fold back, allowing for a cross-sectional view of the film. The observation of these edges by TEM provides an accurate way to measure the number of layers at multiple locations on the film (Fig. 2c-f). Typically, sections of 1–8 layers are observed in our samples, in close agreement with our AFM data. The estimated interlayer spacing is 3.50 ± 0.14 Å. Electron diffraction on the graphene film (inset of Fig. 2a) reveals a hexagonal pattern confirming the three-fold symmetry of the arrangement of carbon atoms (the beam size used was 50 nm). When different regions of the film are inspected, well-defined diffraction spots (instead of ring patterns) are always observed (see Supporting

Information), indicating the crystallinity of all regions examined. Stacking disorder of graphene layers in multilayer regions is suggested by the appearance of electron diffraction spots misaligned with respect to each other (see Supporting Information). Therefore, the observation of lattice fringes (Fig. 2d-f) on the in-plane direction of the graphene sheets is possible. The in-plane lattice constant is measured to be 2.32 ± 0.48 Å (compared to 2.46 Å for graphite[37]).

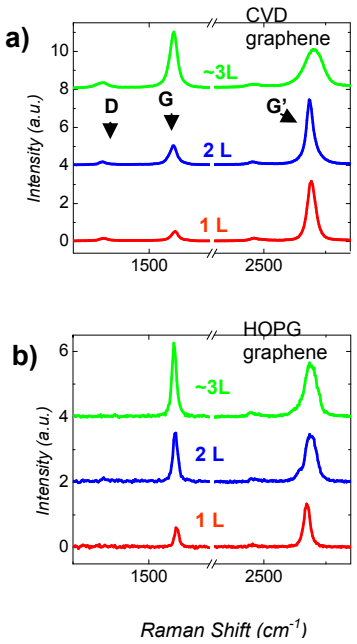

Figure 3. Raman spectroscopy of CVD-grown graphene films on SiO_2/Si. **a**, Raman spectra of 1 (red), 2 (blue) and ~3 (green) graphene layers from a CVD graphene film. **b**, Raman spectra of 1 (red), 2 (blue) and 3 (green) graphene layers derived by the micro-cleaving of HOPG for comparison. The excitation wavelength is 532nm.

Raman spectroscopy provides a quick and facile structural and quality characterization of the produced material. Figure 3 compares the Raman spectra of 1, 2 and 3 graphene layers derived by CVD and by HOPG. A low intensity of the disorder-induced D band (~1350cm^{-1}) is observed (by plotting the D to G (~1580 cm^{-1}) peak intensity ratios (I_D/I_G) where G denotes the symmetry-allowed graphite band) obtaining $0.05<I_D/I_G < 0.3$. Some weak D band intensity is observed also away from graphene edges suggesting the existence of sub-domain boundaries in areas with a constant number of graphene layers. Spectra from the thinnest sections of the CVD graphene film show a sharp linewidth (~30 cm^{-1}) and a single Lorentzian profile of the G' band (~2700 cm^{-1}), which are hallmarks of monolayer graphene [38]. The G' lineshape provides a good measure of the number of layers in the case of HOPG-derived graphene [38]. However, we observe that in multilayer (>1 graphene layers) CVD graphene, there is a variation in the G' lineshape between regions of identical layer number. Moreover, sections of ~2L and 3L regions can show linewidths (~30 cm^{-1}) and Lorentzian. This indicates that an ordered stacking (i.e., ABAB stacking) and therefore an electronic coupling between graphene layers may not occur in all regions of the film, or to the same degree as in HOPG. This observation is consistent with our electron diffraction spectra. The absence of interlayer coupling is not necessarily an adverse effect since incommensurate, multilayer graphene can have electronic properties similar to those of a single sheet of graphene [39]. Instead of the G' lineshape, we have found that the G to G' peak intensity ratios ($I_G/I_{G'}$) provide a good correlation with the number of graphene layers in the CVD graphene samples (see Supporting Information).

The intrinsic quality of the CVD graphene films makes them excellent candidates for both optoelectronic and electronic applications. Figure 4(a) is an optical image of the graphene film transferred onto a glass substrate. With a film having 3nm average thickness, the optical transmittance is ~ 90% in the 500nm to 1000nm wavelength regime (Fig. 4b). The sheet resistances (R_s) of the films are 770 -1000 Ω/sq as measured by a four-point probe instrument. These values compare favorably to graphene films, with similar thickness and transmittance values, fabricated by graphene oxide solution-based methods [10] and are 2 orders of magnitude closer to those of commercial ITO electrodes with the same transparency (120 nm thickness, R_s < 15 Ω/sq.)[17].

We further characterized the electrical properties by fabricating graphene transistors. Photolithography and O_2 plasma etching were used to pattern graphene films in 2μm to 8μm stripes. Transistor channel lengths ranged from 5μm to 15μm. Figure 4c is a histogram of the 2D resistivity obtained by measuring ~ 100 devices at 0V gate voltage. By applying a gate voltage of up to ±40V (provided by a Si back gate with 300nm oxide thickness), the conductance values of the stripes are modulated by 1.3~2 times (Fig. 4d). This indicates that the effect of gate modulation is not as effective as it is in other graphene transistors made by micro-cleaving HOPG[40]. The inset in Fig. 4d shows an optical image of a typical device. The average thickness of the graphene strip of this device is also estimated to be ~ 3 nm. Due to thickness variation, it is possible that the gating effect is screened by other graphene layers in multilayer regions of the film [2, 41]. Mobility values can be derived from the slope of the conductivity variation with gate voltage. These range from 100 to 2000 cm^2/ V sec for both electrons and holes, which are ~2 orders of magnitude lower than the best reported graphene mobilities on substrates. This is possibly due to an ineffective gate

coupling or to grain boundary scattering inside the graphene strip. Efforts are underway to improve the quality of the films by tuning the CVD growth conditions.

The ability to grow single and few-layer graphene with CVD is an important advantage. Analogous to the case of carbon nanotube growth [42, 43], this technique can potentially enable the simple growth of graphene at particular locations and with desired geometries by controlling the catalyst morphology and position[44]. Figure 5 demonstrates the direct CVD growth of a graphene pattern using a pre-patterned Ni structure (Fig. 5a). After CVD, the graphene is transferred to a SiO_2/Si substrate (Fig. 5b) with a process similar to the one described previously (see Supporting Information). This is a significant addition to the capabilities of graphene device fabrication and integration. For example, in the case of O_2 plasma-sensitive substrates or substrates which cannot withstand the lithographic processes, graphene devices can be patterned through this approach.

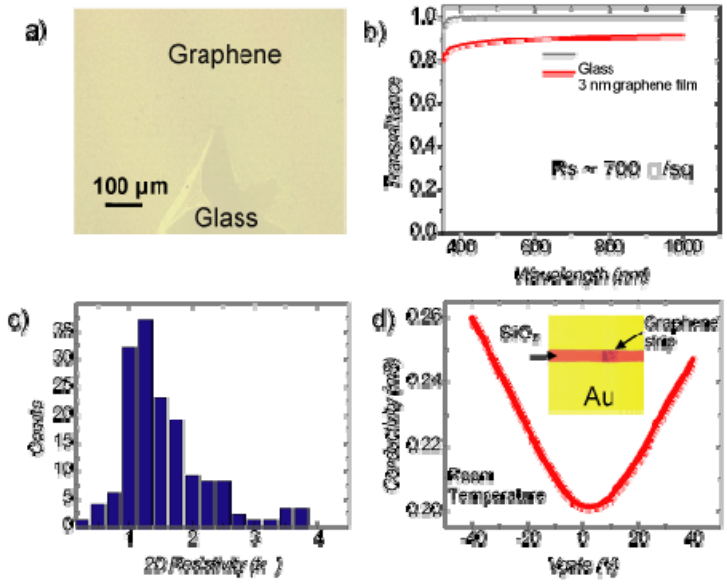

Figure 4. **Optical and electrical characterization of the CVD graphene film and devices**. **a**, Optical image of a graphene film transferred to a glass substrate. The broken edge on the bottom can be used to recognize the film. **b,** Optical transmittance of a graphene film with 3 nm average thickness on glass. **c,** Histogram of the 2D resistivity (kΩ) of ~ 100 graphene film devices prepared by the CVD process. **d,** 2D conductivity vs. gate voltage of a graphene film transistor. An optical image of a graphene strip device is shown as an inset.

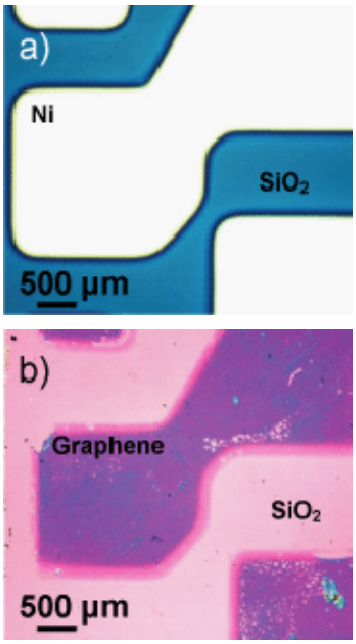

Figure 5. Direct growth of graphene patterns from pre-patterned Ni structures. a, Optical image of a pre-patterned Ni film on SiO_2/Si. CVD graphene is grown on the surface of the Ni pattern. **b,** Optical image of the grown graphene transferred from the Ni surface in (a) to another SiO_2/Si substrate.

In summary, we have demonstrated for the first time that continuous films with single- to few-layer graphene can be grown by ambient pressure CVD on polycrystalline Ni and transferred to a large variety of substrates. The films exhibit a large fraction of single- and bilayer graphene regions with up to ~20 μm in lateral size. They remain continuous and conductive after numerous processing steps, even though the thinnest parts are only one monolayer in thickness. These films demonstrate a comparable structural quality to existing graphene materials but are fabricated without the need of single crystal substrates or complex processing conditions. The graphene film size is determined by the area of the Ni growth surface and is only limited by the CVD chamber size. Furthermore, our studies suggest that the polycrystalline structure of the Ni film plays an important role in the formation of the graphene film morphology. With better engineering of the Ni film, such as enlarging and controlling the location of the single crystal grains, well-controlled graphene features can be envisioned. This approach enables a viable route towards the scalable production of graphene structures for future applications.

REFERENCES

[1] Novoselov, K. S.; Jiang, D.; Schedin, F.; Booth, T. J.; Khotkevich, V. V.; Morozov, S. V.; Geim, A. K., Two-dimensional atomic crystals. *Proceedings of the National Academy of Sciences* **2005,** 102, (30), 10451-10453.

[2] Novoselov, K. S.; Geim, A. K.; Morozov, S. V.; Jiang, D.; Katsnelson, M. I.; Grigorieva, I. V.; Dubonos, S. V.; Firsov, A. A., Two-dimensional gas of massless Dirac fermions in graphene. *Nature* **2005,** 438, (7065), 197-200.
[3] Zhang, Y. B.; Tan, Y. W.; Stormer, H. L.; Kim, P., Experimental observation of the quantum Hall effect and Berry's phase in graphene. *Nature* **2005,** 438, (7065), 201-204.
[4] Schedin, F.; Geim, A. K.; Morozov, S. V.; Hill, E. W.; Blake, P.; Katsnelson, M. I.; Novoselov, K. S., Detection of individual gas molecules adsorbed on graphene. *Nat Mater* **2007,** 6, (9), 652-655.
[5] Oostinga, J. B.; Heersche, H. B.; Liu, X.; Morpurgo, A. F.; Vandersypen, L. M. K., Gate-induced insulating state in bilayer graphene devices. *Nat Mater* **2008,** 7, (2), 151-157.
[6] Ohta, T.; Bostwick, A.; Seyller, T.; Horn, K.; Rotenberg, E., Controlling the electronic structure of bilayer graphene. *Science* **2006,** 313, (5789), 951-954.
[7] Miao, F.; Wijeratne, S.; Zhang, Y.; Coskun, U. C.; Bao, W.; Lau, C. N., Phase-Coherent Transport in Graphene Quantum Billiards. *Science* **2007,** 317, (5844), 1530-1533.
[8] Wang, F.; Zhang, Y.; Tian, C.; Girit, C.; Zettl, A.; Crommie, M.; Shen, Y. R., Gate-Variable Optical Transitions in Graphene. *Science* **2008,** 320, (5873), 206-209.
[9] Bolotin, K. I.; Sikes, K. J.; Jiang, Z.; Klima, M.; Fudenberg, G.; Hone, J.; Kim, P.; Stormer, H. L., Ultrahigh electron mobility in suspended graphene. *Solid State Communications* **2008,** 146, (9-10), 351-355.
[10] Eda, G.; Fanchini, G.; Chhowalla, M., Large-area ultrathin films of reduced graphene oxide as a transparent and flexible electronic material. *Nat Nano* **2008,** 3, (5), 270-274.
[11] Li, D.; Muller, M. B.; Gilje, S.; Kaner, R. B.; Wallace, G. G., Processable aqueous dispersions of graphene nanosheets. *Nat Nano* **2008,** 3, (2), 101-105.
[12] Sutter, P. W.; Flege, J.-I.; Sutter, E. A., Epitaxial graphene on ruthenium. *Nat Mater* **2008,** 7, (5), 406-411.
[13] Berger, C.; Song, Z. M.; Li, X. B.; Wu, X. S.; Brown, N.; Naud, C.; Mayo, D.; Li, T. B.; Hass, J.; Marchenkov, A. N.; Conrad, E. H.; First, P. N.; de Heer, W. A., Electronic confinement and coherence in patterned epitaxial graphene. *Science* **2006,** 312, (5777), 1191-1196.
[14] Liang, X.; Fu, Z.; Chou, S. Y., Graphene Transistors Fabricated via Transfer-Printing In Device Active-Areas on Large Wafer. *Nano Lett.* **2007,** 7, (12), 3840-3844.
[15] Berger, C.; Song, Z. M.; Li, T. B.; Li, X. B.; Ogbazghi, A. Y.; Feng, R.; Dai, Z. T.; Marchenkov, A. N.; Conrad, E. H.; First, P. N.; de Heer, W. A., Ultrathin epitaxial graphite: 2D electron gas properties and a route toward graphene-based nanoelectronics. *Journal of Physical Chemistry B* **2004,** 108, (52), 19912-19916.
[16] Stankovich, S.; Dikin, D. A.; Piner, R. D.; Kohlhaas, K. A.; Kleinhammes, A.; Jia, Y.; Wu, Y.; Nguyen, S. T.; Ruoff, R. S., Synthesis of graphene-based nanosheets via chemical reduction of exfoliated graphite oxide. *Carbon* **2007,** 45, (7), 1558-1565.
[17] Wang, X.; Zhi, L. J.; Mullen, K., Transparent, conductive graphene electrodes for dye-sensitized solar cells. *Nano Letters* **2008,** 8, (1), 323-327.
[18] Li, X.; Zhang, G.; Bai, X.; Sun, X.; Wang, X.; Wang, E.; Dai, H., Highly conducting graphene sheets and Langmuir-Blodgett films. *Nat Nano* **2008,** 3, (9), 538-542.
[19] Hernandez, Y.; Nicolosi, V.; Lotya, M.; Blighe, F. M.; Sun, Z.; De, S.; McGovern, I. T.; Holland, B.; Byrne, M.; Gun'Ko, Y. K.; Boland, J. J.; Niraj, P.; Duesberg, G.; Krishnamurthy, S.; Goodhue, R.; Hutchison, J.; Scardaci, V.; Ferrari, A. C.; Coleman, J. N., High-yield production of graphene by liquid-phase exfoliation of graphite. *Nat Nano* **2008,** 3, (9), 563-568.
[20] Vaari, J.; Lahtinen, J.; Hautojärvi, P., The adsorption and decomposition of acetylene on clean and K-covered Co(0001). *Catalysis Letters* **1997,** 44, (1), 43-49.
[21] Ueta, H.; Saida, M.; Nakai, C.; Yamada, Y.; Sasaki, M.; Yamamoto, S., Highly oriented monolayer graphite formation on Pt(1 1 1) by a supersonic methane beam. *Surface Science* **2004,** 560, (1-3), 183-190.
[22] Starr, D. E.; Pazhetnov, E. M.; Stadnichenko, A. I.; Boronin, A. I.; Shaikhutdinov, S. K., Carbon films grown on Pt(1 1 1) as supports for model gold catalysts. *Surface Science* **2006,** 600, (13), 2688-2695.
[23] Gall', N.; Rut'kov, E.; Tontegode, A., Interaction of silver atoms with iridium and with a two-dimensional graphite film on iridium: Adsorption, desorption, and dissolution. *Physics of the Solid State* **2004,** 46, (2), 371-377.
[24] Coraux, J.; Ndiaye, A. T.; Busse, C.; Michely, T., Structural Coherency of Graphene on Ir(111). *Nano Lett.* **2008,** 8, (2), 565-570.

[25] de Parga, A. L. V.; Calleja, F.; Borca, B.; Passeggi, J. M. C. G.; Hinarejos, J. J.; Guinea, F.; Miranda, R., Periodically Rippled Graphene: Growth and Spatially Resolved Electronic Structure. *Physical Review Letters* **2008,** 100, (5), 056807-4.
[26] Marchini, S.; Gunther, S.; Wintterlin, J., Scanning tunneling microscopy of graphene on Ru(0001). *Physical Review B (Condensed Matter and Materials Physics)* **2007,** 76, (7), 075429-9.
[27] Goodman, D. W.; Yates, J. T., CO isotopic mixing measurements on nickel: Evidence for irreversibility of CO dissociation. *Journal of Catalysis* **1983,** 82, (2), 255-260.
[28] Madden, H. H.; Kuppers, J.; Ertl, G., Interaction of carbon monoxide with (110) nickel surfaces. *The Journal of Chemical Physics* **1973,** 58, (8), 3401-3410.
[29] Gamo, Y.; Nagashima, A.; Wakabayashi, M.; Terai, M.; Oshima, C., Atomic structure of monolayer graphite formed on Ni(111). *Surface Science* **1997,** 374, (1-3), 61-64.
[30] Kawano, T.; Kawaguchi, M.; Okamoto, Y.; Enomoto, H.; Bando, H., Preparation of layered B/C/N thin films on nickel single crystal by LPCVD. *Solid State Sciences* **2002,** 4, (11-12), 1521-1527.
[31] Starodubov, A. G.; Medvetskii, M. A.; Shikin, A. M.; Adamchuk, V. K., Intercalation of silver atoms under a graphite monolayer on Ni(111). *Physics of the Solid State* **2004,** 46, (7), 1340-1348.
[32] Reina, A.; Son, H.; Jiao, L.; Fan, B.; Dresselhaus, M. S.; Liu, Z.; Kong, J., Transferring and Identification of Single- and Few-Layer Graphene on Arbitrary Substrates. *J. Phys. Chem. C* **2008**.
[33] Abergel, D. S. L.; Russell, A.; Fal'ko, V. I., Visibility of graphene flakes on a dielectric substrate. *Applied Physics Letters* **2007,** 91, (6), 063125-3.
[34] Blake, P.; Hill, E. W.; Neto, A. H. C.; Novoselov, K. S.; Jiang, D.; Yang, R.; Booth, T. J.; Geim, A. K., Making graphene visible. *Applied Physics Letters* **2007,** 91, (6), 063124-3.
[35] Gupta, A.; Chen, G.; Joshi, P.; Tadigadapa, S.; Eklund, P. C., Raman scattering from high-frequency phonons in supported n-graphene layer films. *Nano Letters* **2006,** 6, (12), 2667-2673.
[36] Li, X.; Wang, X.; Zhang, L.; Lee, S.; Dai, H., Chemically Derived, Ultrasmooth Graphene Nanoribbon Semiconductors. *Science* **2008,** 319, (5867), 1229-1232.
[37] Baskin, Y.; Meyer, L., Lattice Constants of Graphite at Low Temperatures. *Physical Review* **1955,** 100, (2), 544.
[38] Ferrari, A. C.; Meyer, J. C.; Scardaci, V.; Casiraghi, C.; Lazzeri, M.; Mauri, F.; Piscanec, S.; Jiang, D.; Novoselov, K. S.; Roth, S.; Geim, A. K., Raman Spectrum of Graphene and Graphene Layers. *Physical Review Letters* **2006,** 97, (18), 187401-4.
[39] Hass, J.; Varchon, F.; Millan-Otoya, J. E.; Sprinkle, M.; Sharma, N.; de Heer, W. A.; Berger, C.; First, P. N.; Magaud, L.; Conrad, E. H., Why Multilayer Graphene on 4H-SiC(000[overline 1]) Behaves Like a Single Sheet of Graphene. *Physical Review Letters* **2008,** 100, (12), 125504-4.
[40] Chen, J.-H.; Jang, C.; Xiao, S.; Ishigami, M.; Fuhrer, M. S., Intrinsic and extrinsic performance limits of graphene devices on SiO2. *Nat Nano* **2008,** 3, (4), 206-209.
[41] Novoselov, K. S.; Geim, A. K.; Morozov, S. V.; Jiang, D.; Zhang, Y.; Dubonos, S. V.; Grigorieva, I. V.; Firsov, A. A., Electric Field Effect in Atomically Thin Carbon Films. *Science* **2004,** 306, (5696), 666-669.
[42] Kong, J.; Soh, H. T.; Cassell, A. M.; Quate, C. F.; Dai, H., Synthesis of individual single-walled carbon nanotubes on patterned silicon wafers. *Nature* **1998,** 395, (6705), 878-881.
[43] Hayamizu, Y.; Yamada, T.; Mizuno, K.; Davis, R. C.; Futaba, D. N.; Yumura, M.; Hata, K., Integrated three-dimensional microelectromechanical devices from processable carbon nanotube wafers. *Nat Nano* **2008,** 3, (5), 289-294.
[44] E. Sutter, P. S., Au-Induced Encapsulation of Ge Nanowires in Protective C Shells. *Advanced Materials* **2006,** 18, (19), 2583-2588.

2. Softening of the Radial Breathing Mode in Metallic Carbon Nanotubes

Sponsors
Materials, Structure and Devices (MSD) Center, one of the five programs in the focus center research program (FCRP), a Semiconductor Research Corporation program. Raman measurements were carried out in the George R. Harrison Spectroscopy Laboratory supported by NSF-CHE 0111370 and NIH-RR02594. M. S.D. was supported by NSF/DMR 07-04197 and R. S. by MEXT Grants (No. 20241023 and No. 16076201).

Project Staff
H Farhat, K. Sasaki, M. Kalbac, M. Hofmann, R. Saito, M. S. Dresselhaus, and J. Kong

The softening of the radial breathing mode (RBM) of metallic single walled carbon nanotubes (m-SWNTs) due to electron-phonon coupling has been studied by observing the Fermi level (ϵ_F) dependence of the RBM Raman peak. *In situ* Raman spectra were obtained from several individual m-SWNTs while varying ϵ_F electrochemically. The RBM frequency of an intrinsic m-SWNT is shown to be downshifted relative to highly doped tubes by ~2 cm^{-1}. The down-shift is greatest for small diameter and small chiral angle SWNTs. Most tubes show no change in RBM linewidth. A comparison is drawn between the RBM and the G band (A_{LO} phonon) with respect to the ϵ_F dependence of their frequencies and linewidths.

Electron-phonon (*e*-ph) interactions govern many aspects of the physical properties of materials. In graphene and single walled carbon nanotubes (SWNTs), the coupling between electrons and the in-plane C-C stretching optical phonon modes (*G*-band phonons) influences the phonon structure [1,2], electrical transport [3], and optical transition properties of these materials [4]. Thus, significant effort has been devoted to this subject recently. Another phonon mode of interest in SWNTs is the isotropic radial deformation of the nanotube called the radial breathing mode (RBM). This optical phonon is solely the result of the one-dimensional tubular structure of SWNTs and its deformations are very different from those of the optical stretching modes that are common to all other graphitic materials. *e*-ph coupling of the RBM is important because it provides a new scattering channel for electrons that is absent in higher dimensional forms of carbon. Being a low energy optical phonon, the RBM could be a significant scatterer of low energy electrons such as in electrical transport at low biases [5].

In metallic SWNTs (m-SWNTs) *e*-ph coupling can be especially strong because a wide range of phonon energies is able to resonantly excite electrons across the linear electronic bands. Phonons that effectively couple to excitations near the Fermi surface experience lifetime broadening and energy renormalization [1,2]. This phenomenon is typically investigated by studying how the phonon energy and lifetime evolve as a function of the Fermi energy, ϵ_F. For the G^- Raman peak of a m-SWNT, the observed up-shift and narrowing of the peak with doping has helped clarify the origin of the metallic G-band line shape and the role of electronic excitations in the softening of the A_{LO} phonon at ϵ_F for the neutral m-SWNT [6]. A recent theoretical treatment of the ϵ_F dependence of the RBM predicts a similar, albeit weaker, softening of the RBM phonon with a significantly larger chiral angle dependence [7]. Because the RBM energy is so much smaller than the G band, the *e*-ph coupling is expected to be much more sensitive to the fine structure of the electronic bands near the Dirac point where the valence and conduction bands touch. An experimental study of the softening of the RBM frequency in m-SWNTs is therefore important to clarify the structure-dependent *e*-ph coupling phenomena associated with the RBM phonon.

In this Letter we present a careful analysis of the frequency ω_{RBM} and linewidth γ_{RBM} of the RBM of individual SWNTs as a function of the electrochemical gating potential V_g.We observe an increase in frequency when the nanotube is doped with either electrons or holes. Our experimental results show a diameter (d_t) and chiral angle (θ) dependence of the ω_{RBM} softening.

We use a transparent polymer electrolyte (PEO=$LiClO_4$) to electrochemically dope m-SWNTs. Long, gas flow aligned SWNTs are grown by chemical vapor deposition and then contacted by a Cr=Au electrode to form the working electrode of the electrochemical cell. The SWNTs are typically several hundred microns long and are separated from each other by 20–50 μm. A Pt counter electrode is controlled by a Princeton Applied Research 283 potentiostat to vary the potential (V_g) of an Ag pseudoreference electrode with respect to the SWNTs [8]. Raman measurements are made through the transparent electrolyte. The nanotube metallicity is determined by placing ω_{RBM} and the excitation energy E_{laser} on a Kataura plot, and by observing a broadening and shift of the G band [6]. The m-SWNTs under study are either isolated or in small bundles of two or three SWNTs. However, only one SWNT contributes to the signal for these measurements.

Figure 1(a) shows the RBM spectrum of a m-SWNT at several values of V_g. Here, a positive (negative) V_g corresponds to electron (hole) doping. A subtle up-shift of 2 cm^{-1} for both (±) polarities of V_g is observed. Changes in ω_{RBM} are more evident after fitting the peaks, whereby the fit gives both ω_{RBM} and the FWHM linewidth γ_{RBM} versus V_g, shown in Figs. 1(b) and 1(c), respectively. We use a Voigt profile to deconvolute the instrumental broadening from the Lorentzian linewidth of the RBM peak. The ω_{RBM} of the m-SWNT shown in Fig. 1(b) makes an almost symmetric ''*V*'' shape about V_g = 0. Previous studies suggest that environmental effects such as the van der Waals interaction of the SWNT with the substrate or

surrounding solution may modify ω_{RBM} [9]. The latter effect presumably only contributes to a constant background with respect to V_g. The large drop in the peak intensity observed with increasing V_g may be caused by a change in the resonance condition. Because of the loss in peak intensity with increasing V_g, we are only able to follow ω_{RBM} (V_g) for those m-SWNTs that have strong signals, which biases our sample set towards tubes with small θ values [7]. These m-SWNTs all exhibit a similar characteristic ω_{RBM} (V_g) behavior. Meanwhile, the RBM peak for a semiconducting SWNT (s-SWNT) shows no appreciable change in ω_{RBM} (V_g) as a function of V_g, as, for example, shown in the inset of Fig. 1(b). It is thus clear that the behavior in Fig. 1(b) is an effect specific to m-SWNTs.

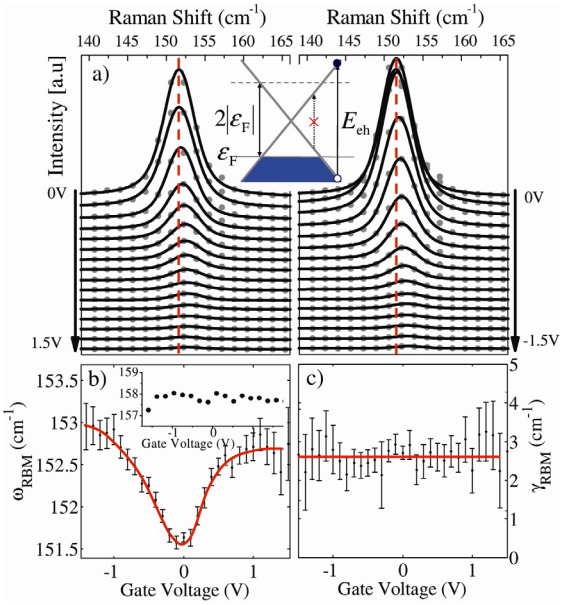

Figure 1: (a) Waterfall plots of the RBM spectra of a m-SWNT at several positive (left-hand panel) and negative (right-hand panel) values of gate potential V_g. To evaluate the ω_{RBM} down-shift we use the vertical red lines as fiduciary marks indicating the peak frequency at V_g = 0. The inset of (a) is a schematic band structure of a m-SWNT illustrating the allowed *e-h* transitions. **(b)** Fitted frequency ω_{RBM} and **(c)** FWHM linewidth γ_{RBM} values versus V_g. Error bars denote 95% confidence interval. Solid curves guide the eye. The inset of (b) shows the fitted ω_{RBM} (V_g) for a s-SWNT.

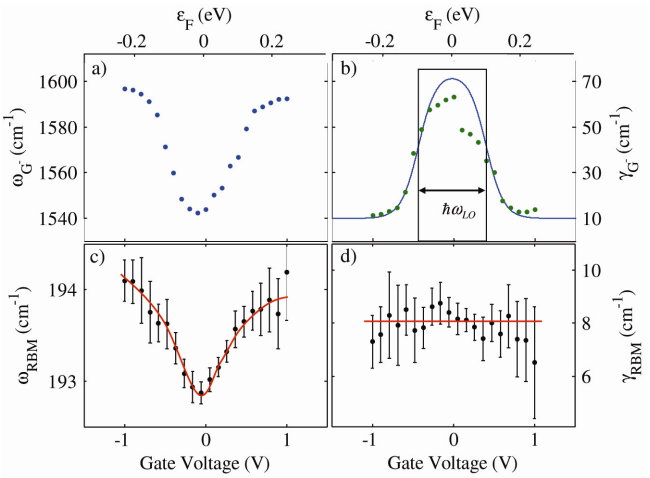

Figure 2: Comparing the G^- and RBM peaks versus V_g for a (13,4) m-SWNT (ω_{RBM} ~ 193 cm^{-1}, E_{laser} = 1:91 eV). (a) the G_ frequency and (b) G^- linewidth versus V_g (bottom axis) and $\in_F$ (top axis). The V_g dependence of the γ_G is used to estimate the gating efficiency, α = 0:24 eV/V. The box in **(b)** gives the T = 0 energy range within which the LO phonon can excite real *e-h* pairs. **(c)** ω_{RBM} and **(d)** γ_{RBM} for the same m-SWNT.

The behavior of ω_{RBM} for m-SWNTs can be understood by considering that, like the G-band phonons, the RBM is also an optical phonon capable of exciting vertical electron-hole (*e-h*) pairs across the linear *k* valence and conduction bands of the m-SWNT near the K (or K0) point. If the *e*-ph matrix element for such transitions is nonzero, these scattering events contribute to renormalizing the phonon energy and decreasing its lifetime. As illustrated in the inset of Fig. 1(a), the Pauli exclusion principle limits the available *e-h* pair transitions to those satisfying $E_{e\text{-}h} > 2|\in_F|$, thus giving rise to the V_g dependence of ω_{RBM}. As $\in_F$ is shifted away from the Dirac point, the number of excitations contributing to the *dressed* RBM phonon is reduced and ω_{RBM} approaches the frequency of the *bare* RBM phonon [7].

In Fig. 2 we compare the $\in_F$ dependence of the G^- peak (A_{LO} phonon) to ω_{RBM} of a m-SWNT which we tentatively assign as a (13,4) SWNT (ω_{RBM} = 193 cm^{-1}, E_{laser} = 1:91 eV). We see a striking resemblance between the V_g dependence of ω_G- and that of, with both peaks displaying a minimum in frequency around V_g = 0. However, the ω_{RBM} behavior of the two peaks is quite different with the RBM peak showing no noticeable broadening in contrast to the 60 cm^{-1} broadening of the G^- peak. The lack of broadening for the RBM indicates a negligible resonant decay of the RBM into an *e-h* pair.

To understand why the RBM is down-shifted but not broadened, it is instructive to draw comparisons to the *e*-ph coupling of the optical phonons that contribute to the *G* band of graphene, m-SWNTs and s-

SWNTs, which have recently been studied in great detail [6,10–13]. In m-SWNTs, the LO phonon (with energy 0.2 eV) is able to create real and virtual *e-h* pairs across the linear electronic bands, resulting in the strong broadening and downshift in frequency characteristic of the metallic G^- peak as shown in Fig. 2. Similarly, in graphene, the *G*-band phonons are both broadened and down-shifted because they couple to *e-h* excitations near the Dirac point. In the case of s-SWNTs, the optical phonons do not have sufficient energy to excite *e-h* pair excitations across the large electronic energy gap. However, these optical phonons can still create virtual excitations which contribute to the downshift of the phonon frequency. Since there is no decay into real states, there is no linewidth broadening and the frequency shift is modest compared to that of m-SWNTs, as recently verified in experiments [13,14].

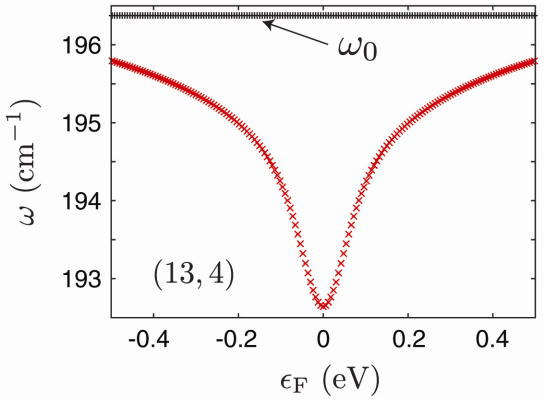

Figure 3: Calculated ω_{RBM} versus $\in_F$ for a (13,4) m-SWNT. For this m-SWNT the *e*-ph coupling contribution to the γ_{RBM} is zero. Black points ω_0 give the bare ω_{RBM} and gray (red) points give the corrected ω_{RBM} [7].

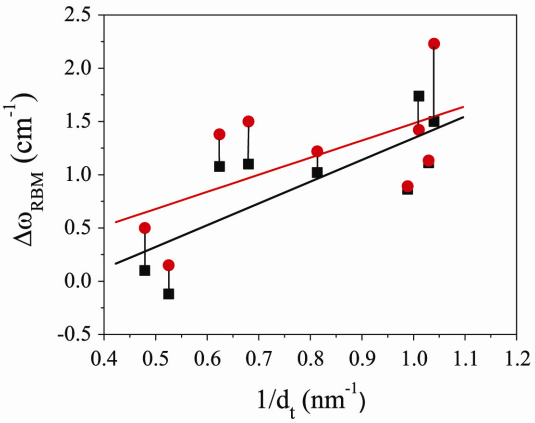

Figure 4: The down-shift $\Delta\omega_{RBM}$ in ω_{RBM} vs $1/d_t$. Red circles indicate the shift relative to $V_g = V_0 - 1V$ (hole doping) and black squares indicate the shift relative to $V_g = V_0 + 1V$ (electron doping). Solid lines represent linear fits to the experimental data points.

Since $\hbar\omega_{RBM}$ is a small fraction of the LO/TO phonon energies, the *e-h* excitations for the RBM occur much closer to the Dirac point. On this energy scale a very small energy gap, such as the curvature-induced minigap, becomes significant. The latter, given by $E_{GAP} = \left(A/d_t^2\right)\times\cos(3\theta)$, is greatest for zigzag and absent for armchair m-SWNTs. The value of *A* is about 60 meV based on an extended tight-binding model [7]. From the perspective of the RBM phonon, the electronic bands of small diameter zigzag m-SWNTs with $E_{gap} > \hbar\omega_{RBM}$ appear semiconductinglike. Only the armchair SWNTs have truly metallic bands when close to the Dirac point. Indeed, for the (13,4) SWNT shown in Fig. 2, E_{gap} = 32 meV (d_t = 1:2 nm, θ = 13°) exceeds the $\hbar\omega_{RBM}$ (24 meV) and hence no linewidth broadening is expected.

In Fig. 3 we show ω_{RBM} for the (13,4) nanotube calculated from the effective mass theory in [7], which also predicts no change in γ_{RBM} as a function of $\in_F$ and a ω_{RBM} behavior qualitatively similar to what we observe in our measurements. For a quantitative comparison, we converted the V_g scale of Fig. 2 to an energy scale (bottom axis) using a gate efficiency of α = 0.24 (eV/V). The α value is determined by fitting the broadening window of the G^- peak to $\gamma_{G-} = \gamma_o + \gamma_{EPC}(V_g)$, as shown in Fig. 2(b). Here, γ_{EPC}, the linewidth due to *e*-ph coupling, is given by Eq. (29) of [1]. The V_g independent contributions to the linewidth are included in γ_o which is taken as 10 cm^{-1} based on our experimental results. Comparing Fig. 2(c) with Fig. 3 within the same $\in_F$ range, we see that the experimental shift of ω_{RBM} is approximately a factor of 2 smaller than that predicted.

It is important to know in what d_t range the softening of ω_{RBM} becomes significant. The down-shift in ω_{RBM} is greatest in smaller d_t m-SWNTs as seen in Fig. 4, which plots the observed frequency down-shift relative to $V_g = V_0 + 1V$ (black) and relative to $V_g + V_0 - 1V$ [gray (red)] as a function of $1/d_t$ for several m-SWNTs, where V_0 is the gate voltage where the minimum in frequency occurs. The *e*-ph matrix element and hence the frequency shift $\Delta\omega_{RBM}$ at a constant V_g is expected to be linear in 1=dt [7]. The experimental data increase monotonically versus 1=dt with some variation that we attribute to the expected _ dependence of ω_{RBM} [7]. Note that the shift on the negative gate side is in most cases greater than it is on the positive side. We attribute the mild asymmetry with respect to the sign of V_g to the C-C

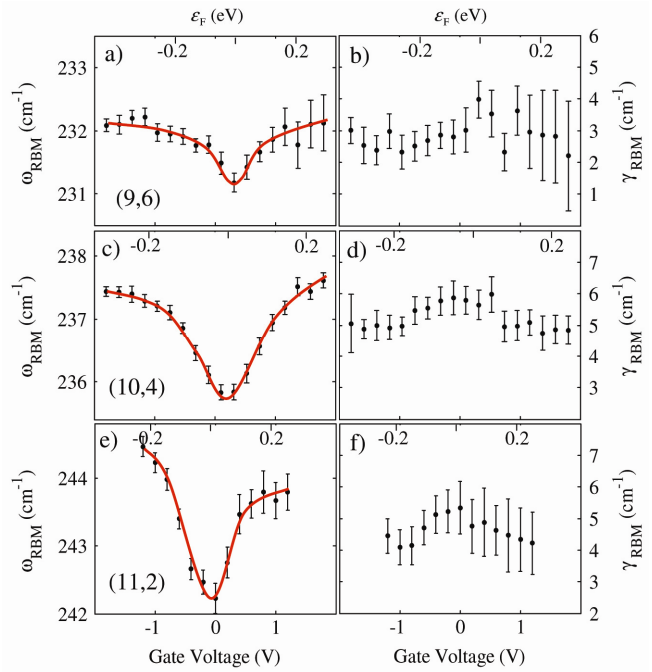

Figure 5: Fitted ω_{RBM} and γ_{RBM} for three m-SWNTs from family $2n+m=24$. **(a),(b)** (9,6); **(c), (d)** (10,4); **(e),(f)** (11,2). The curvature-induced energy gaps for the three m-SWNTs are 19.3, 41.7, and 60.5 meV, respectively. The energy scale (top axis) is estimated for each m-SWNT as in Fig. 2. Solid red lines are curves to guide the eye.

bond softening (stiffening) due to charging the lattices with electrons (holes). There may also be a difference in the gating efficiency for $\pm V_g$.

To further explore the θ dependence of ω_{RBM} we have measured the V_g dependence of three consecutive m-SWNTs from the $2n + m = 24$ family, namely, (11,2), (10,4), and (9,6) as shown in Fig. 5. For a given V_g, the magnitude of the measured $\Delta\omega_{RBM}$ decreases from the (11,2) to the (9,6) nanotube. This is in agreement with the predicted θ dependence of the down-shift in ω_{RBM} [7]. The *e*-ph matrix element, given approximately by $\langle e\text{-}h|H_{e\text{-}ph}|\mathrm{RBM}\rangle = g(|s_z|/d_t)\cos(3\theta)$, where g is the off-site *e*-ph coupling constant and s_z is the radial displacement, is greatest for the zigzag m-SWNT and approaches zero for the armchair m-SWNT [7]. Consequently the zigzag RBM is expected to exhibit the largest frequency shift but no broadening, while the armchair RBM should show neither a change in ω_{RBM} nor in γ_{RBM}. An intermediate chiral m-SWNT could be expected to exhibit both a frequency shift and a broadening. Within the $2n + m = 24$ family, only the (9,6) and (8,8) tubes have a RBM phonon which is greater in energy than the curvatureinduced band gap. As shown in Ref. [7], the (9,6) tube is expected to exhibit a broadening $\Delta\gamma = 2$ cm^{-1} and a negligible frequency shift at 300 K. However, we observe a small frequency shift and no change in linewidth. On the other hand, the (10,4) SWNT is not expected to exhibit any broadening, but we observe a possible small broadening of $\Delta\gamma = 1$ cm^{-1}. Besides these deviations, the overall measured d_t and θ dependences of the ω_{RBM} down-shift are in good qualitative agreement with Ref. [7].

It should be noted that the energy gaps for the (9,6) and (10,4) nanotubes are only 7 meV below and 15 meVabove their RBM phonon energies, respectively. The ω_{RBM} and γ_{RBM} of m-SWNTs are predicted to depend strongly on the position of the cutting line with respect to the *K* point, as well as on the size of the energy gap with respect to the $\hbar\omega_{RBM}$. Small perturbations to the lattice such as strain [15], the displacement of the A_{LO} phonon [16,17], and breaking of mirror symmetry [18] could sufficiently change the electronic structure to alter the $\in_F$ dependence of the RBM peak.

In summary, we have experimentally confirmed that there is a mild softening of the ω_{RBM} of m-SWNTs which can be removed by both positive and negative doping. The magnitude of the down-shift scales with $1/d_t$, and is largest for small θ. The measured ω_{RBM} shifts agree qualitatively with the curvature-dependent softening in Ref. [7]. No gate-induced change in γ_{RBM} is found for most of the SWNTs that we studied, as is expected [7] for small (d_t) SWNTs. Our result shows that chirality dependent corrections to ω_{RBM} are required to better assign the d_t and (n,m) indices for small d_t m-SWNTs, and that environmental doping can be responsible for some of the variability in the observed ω_{RBM}. This work also implies that the role of the RBM in electrical transport and other phonon assisted relaxation processes warrants further investigation.

REFERENCES

[1] N. Caudal et al., Phys. Rev. B 75, 115423 (2007).
[2] K. Sasaki et al., Phys. Rev. B 77, 245441 (2008).
[3] Z. Yao, C. L. Kane, and C. Dekker, Phys. Rev. Lett. 84, 2941 (2000).
[4] S. G. Chou et al., Phys. Rev. B 72, 195415 (2005).
[5] V. Perebeinos, J. Tersoff, and P. Avouris, Phys. Rev. Lett. 94, 086802 (2005).

[6] H. Farhat et al., Phys. Rev. Lett. 99, 145506 (2007).
[7] K. Sasaki et al., Phys. Rev. B 78, 235405 (2008).
[8] The gate potential Vg ¼_Ve, where Ve is the electrochemical potential, defined as the potential of the working electrode with respect to the reference electrode.
[9] P. T. Araujo et al., Phys. Rev. B 77, 241403(R) (2008).
[10] J. Yan, Y. Zhang, P. Kim, and A. Pinczuk, Phys. Rev. Lett. 98, 166802 (2007); S. Pisana et al., Nature Mater. 6, 198 (2007).
[11] K. T. Nguyen, A. Gaur, and M. Shim, Phys. Rev. Lett. 98, 145504 (2007).
[12] Y. Wu et al., Phys. Rev. Lett. 99, 027402 (2007).
[13] J. C. Tsang et al., Nature Nanotech. 2, 725 (2007).
[14] M. Kalbac et al., Nano Lett. 8, 3532 (2008).
[15] M.Y. Huang et al., Phys. Rev. Lett. 100, 136803 (2008).
[16] O. Dubay, G. Kresse, and H. Kuzmany, Phys. Rev. Lett. 88, 235506 (2002).
[17] G. G. Samsonidze et al., Phys. Rev. B 75, 155420 (2007).
[18] M. Ouyang, J. L. Huang, C. L. Cheung, and C. M. Lieber, Science 292, 702 (2001).

3. Electroluminescence from suspended and on-substrate metallic single-walled carbon nanotubes

Sponsors
Partial support by the Materials, Structure and Device Center, one of the five centers of the Focus Center Research Program (FCRP) and NSF/DMR 07-04197. LM Xie acknowledges a Scholarship from China Scholarship Council, the Peking University CDY Scholarship and NSFC (20725307, 20808004).

Project Staff
Liming Xie, Hootan Farhat, Hyungbin Son, Jin Zhang, Mildred S. Dresselhaus,, Jing Kong, Zhongfan Liu

In this work, we carried out electroluminescence (EL) measurements on metallic single-walled carbon nanotubes (SWNTs) and compared the light emission from the suspended section and the on-substrate section along the same SWNT. In addition to the lowest excitonic emission for metallic SWNTs (M_{11}), a side peak was observed at an energy of 0.17- 0.20 eV lower than the M_{11} peak, which is attributed to a phonon-assisted sideband. Interestingly, this side peak was only observed from on-substrate sections but not from suspended sections. This is likely due to the higher electric field used in the EL measurement of on-substrate sections and the asymmetric surroundings for on-substrate SWNT sections. When the drain voltage is increased, either a blue shift or a red shift of the M_{11} emission (up to ±20 meV) was observed in different suspended SWNTs. The red shift can be explained by the temperature-dependence of the M_{11} transition energy, whereas the blue shift is surprising and has never been observed before. Some possible mechanisms for the blue shift are discussed.

With their unique electronic properties and one-dimensional structure, single-walled carbon nanotubes (SWNTs) have potential applications in future nanoelectronics and nanophotonics. Photoluminescence (PL) and electroluminescence (EL) have been intensively investigated to understand the fundamental photophysics in SWNTs[1-6]. In both PL and EL studies, substrates have played an important role in influencing the properties of SWNTs[2, 7-9]. Up to now, PL has not been observed from semiconducting SWNTs directly grown on substrates[2], and suspended semiconducting SWNTs gives a much higher PL efficiency[10] than surfactant-wrapped semiconducting SWNTs[5]. On the other hand, EL has been observed from all SWNTs (semiconducting or metallic, suspended or on-substrate)[1, 4, 11]. Thus EL is especially useful to investigate the fundamental photophysics of metallic SWNTs as well as substrate effects. Since the EL properties of different SWNT devices (either suspended or on-substrate) are dramatically different[1, 3, 4], comparing the EL spectra from suspended and on-substrate sections from the same SWNT will be very useful to provide further insight into the fundamental physics in SWNTs.

In the present work, we measured the EL emission from suspended and on-substrate sections along the same metallic SWNT (Figure 1). While the suspended section exhibits a stronger EL signal at a given drain voltage V_{ds} and the signal can be clearly observed at a lower V_{ds}, the on-substrate section has an additional side peak at 0.17-0.20 eV below the lowest excitonic transition (M_{11}). This side peak is assigned to phonon-assisted emission. Moreover, in suspended sections, we have observed an interesting blue shift of the EL emission energy at higher drain voltages, which cannot be explained by the temperature dependence of the transition energy M_{11}.

Devices with on-substrate and suspended sections along the same long individual SWNTs were fabricated either by transfer[12] or by direct chemical vapor deposition (CVD) growth of ultra-long SWNTs[13] on substrates pre-fabricated with trenches and electrode patterns. These substrates are the same as those used in reference[11]. Briefly, a Si_3N_4 film (thickness ~ 38 nm) was deposited on a SiO_2/Si wafer (t_{ox} = 500 nm). And then trenches were fabricated by photolithography and etching. Finally Pt electrodes (thickness ~ 25 nm) were deposited. The CVD growth of ultra-long SWNTs was carried out by an Fe-assisted ethanol CVD method[13]. The SWNT transfer was done by a PMMA-mediated transfer method[12]. The EL measurement was achieved by a home-built setup. A 50x aspheric lens was used to collect the EL signal, and a 300 line/mm grating and a 512-pixel InGaAs detector (Hamamatsu G9204-512D, spectrum range 900-1700 nm) were used to disperse the light and record the spectra. A typical spectrum integration time of 60 to 120 s was used for collecting the spectra. All EL measurements were conducted under an Argon atmosphere.

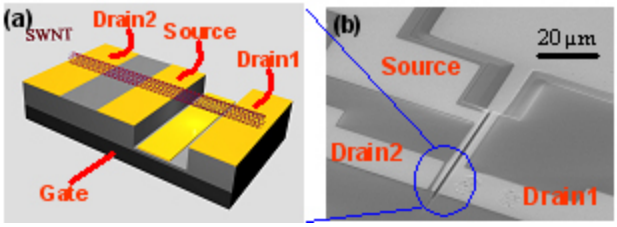

Figure 1. Schematic illustration **(a)** and scanning electron microscopy image **(b)** of suspended and on-substrate devices fabricated along the same SWNT.

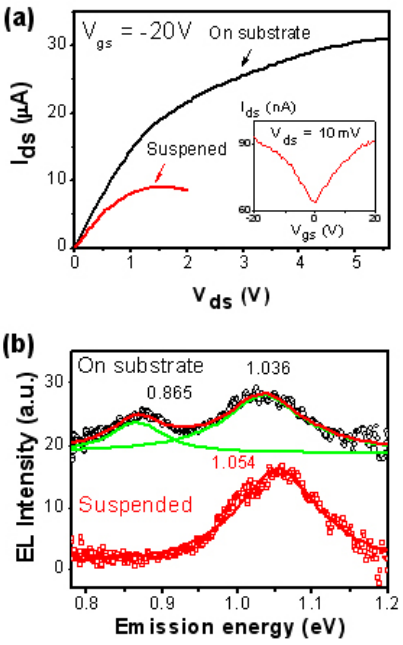

Figure 2. (a) Drain current (I_{ds}) versus drain voltage (V_{ds}) plot for suspended (red line) and on-substrate (black line) sections along the same SWNT. The inset shows the drain current vs. gate voltage (V_{gs}) plot of the suspended section. **(b)** Electroluminescence (EL) from the suspended section (red circle) at V_{ds} = 2.0 V and the on-substrate section (black circle) at V_{ds} = 5.6 V. A gate voltage V_{gs} = -20 V is used in all EL measurements. Data are offset for clarity. Red lines are a Lorentzian fit to the results and green lines are fit curves for the individual peaks.

Figure 1a is a schematic illustration of our metallic SWNT devices with one section on the Si_3N_4 substrate and the other section suspended. Figure 1b is a scanning electron microscope (SEM) image of a typical device. In our experiments, doped Si was used for the gate (back gate). The channel lengths of the devices are about 1 μm. The trench depth is about 300 nm. Figure 2a shows a typical drain-source current I_{ds} vs. drain-source voltage V_{ds} plot of our devices. For the on-substrate section, I_{ds} saturates at high V_{ds} due to electron scattering by optical phonons[9], whereas for the suspended section, a negative differential conductance occurs at V_{ds}>1.2 V. The inset in Figure 2a shows the drain current I_{ds} vs. gate voltage (V_{gs}) curve (under constant bias voltage V_{ds} = 10 mV) for the same SWNT (the suspended section), which is a typical I_{ds}-V_{gs} curve for a metallic SWNT. In our experiments, in order to measure EL from individual SWNT devices but not from multi-walled carbon nanotube devices or nanotube-bundle devices, we used the nanotube devices in which the on-substrate sections have saturation currents of about 25 μA.[14, 15] The EL spectra from this SWNT are presented in Figure 2b. For the suspended section, only one EL peak was observed with a value of 1.054 eV at V_{ds} = 2.0 V and V_{gs} = -20 V. Using the diameter information (~2.3 nm) obtained by atomic force microscopy (AFM) measurements, the 1.054 eV peak from the suspended section can be assigned to the M_{11} excitonic transition[16]. There could be an emission component from the M_{11} continuum which is embedded in the M_{11} exciton emission since the exciton binding energy (~30 meV for 2.3-nm diameter metallic SWNTs, estimated from the 50 meV reported for a (10,10) SWNT[17]) is less than both the thermal energy (>60 meV[11]) and the EL emission peak width (~100 meV).

In contrast, for the on-substrate section, two EL peaks (0.865 and 1.036 eV) were observed. Measurements from two other SWNT devices showed similar phenomena, namely, the suspended sections only displayed the M_{11} emissions, whereas the on-substrate sections exhibited two emission peaks, one dominant peak near M_{11} of the suspended section and the other one lying 0.17-0.20 eV lower

in energy. For the on-substrate sections, a higher V_{ds} is required for observable EL emission. Since the exciton binding energy for a 2.3nm diameter metallic SWNT is about 30 meV, the two peaks in the emission spectrum of the on-substrate section cannot together be identified with an M_{11} exciton transition and an M_{11} continuum. Additionally, the two peaks also cannot be the energy splitting of the M_{11} transition due to trigonal warping because this splitting is less than 70 meV for a 2.3nm diameter metallic SWNT[18]. Considering that the energy difference between the two peaks (~0.17 eV) is close to a Γ-point optical phonon energy (~0.2 eV) and a K-point phonon energy (0.16 eV), the lower energy side peak is assigned to an optical phonon-assisted emission (either from the Γ or K point. From our later discussion, it appears that a Γ-point optical phonon-assisted emission is more likely). Thus the peak at higher energy is assigned to the M_{11} emission. Additionally, compared with that from the suspended section, a red-shift (downshift) of 18 meV for the M_{11} emission from the on-substrate section was found and this downshift will be discussed later.

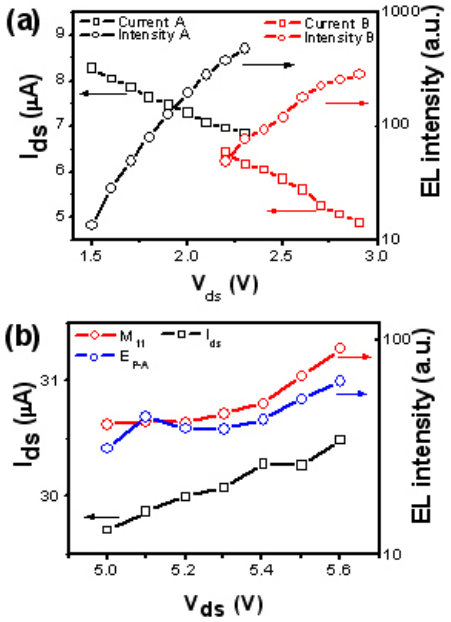

Figure 3. (a) Drain current (I_{ds}) and EL intensity plot vs. drain voltage (V_{ds}) for two suspended SWNTs A and B. **(b)** Drain current (I_{ds}) and EL intensity plot vs. drain voltage (V_{ds}) for the same on-substrate section of the SWNT used in Figure 2. M_{11} and E_{P-A} denote the lowest excitonic transition and phonon-assisted emission, respectively.

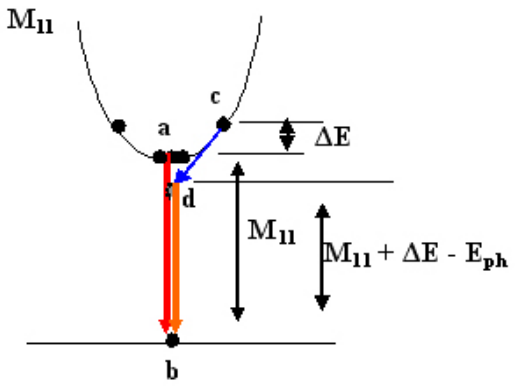

Figure 4. Schematic diagram for direct M_{11} emission (a→b) and phonon-assisted emission (c→d→b). Black dots denote excitons. The phonon-assisted emission energy is M_{11} + ΔE – E_{ph}, where M_{11} is the lowest excitonic transition energy for metallic SWNTs and ΔE is the average energy difference between the excitons at 'c' and the excitons at 'a', and E_{ph} is the phonon energy.

The drain current and emission intensity vs. drain voltage are plotted in Figure 3. For suspended sections, similar to the previous observation in reference[11], EL was observed in the negative differential conductance region, where I_{ds} decreases with V_{ds} and the EL intensity increases with V_{ds} (Figure 3a). In contrast to the suspended SWNTs, I_{ds} for the on-substrate SWNT section used in Figure 2 continues to increase with V_{ds} under a large bias of up to 5.6 V, as shown in Figure 3b. But the EL intensity dependence on V_{ds} for the on-substrate section is different from that observed for the suspended sections. The emission intensity for both the phonon-assisted transition (E_{P-A}) and the M_{11} emission for the on-substrate section increased slowly in the range V_{ds} = 5.0- 5.4 V and then increased more rapidly in the range V_{ds} = 5.4- 5.6 V.

Now we move our attention to the origin of the phonon-assisted emissions. This phonon-assisted side band was only observed from the on-substrate sections. Before discussing this difference, the EL mechanisms for suspended and on-substrate SWNTs should be discussed in more detail. Previous works[11, 19] have shown that the EL from suspended metallic SWNTs is via a thermal light emission mechanism. In this case, hot electrons are thermally distributed in higher energy bands. However, for on-substrate metallic SWNTs, no EL mechanism has previously been reported. Since suspended SWNTs

give observable thermal light emission above 800 K[11], and on-substrate metallic SWNTs can be heated up to 900 K in air before they are burnt out[20] (in an Ar atmosphere, the same on-substrate SWNT devices can go up to an even higher V_{ds}, indicating that on-substrate SWNTs can go up to a higher temperature), thermal light emission should also be possible for on-substrate metallic SWNTs. Impact excitation, which occurs under a high electrical field[1, 21], is also another possible mechanism for EL emission from on-substrate metallic SWNTs. The average electrical field in our EL experiment is about 5 V/μm. The electrical field in the regions of the contacts, defects and impurities may be higher.

For the energy difference between the side band and the M_{11} emission, two other SWNTs give an energy difference of 0.20 and 0.17 eV. Since different excitons in 1nm diameter semiconducting SWNTs only have an energy difference of <40 meV[22, 23] and the exciton binding energy in metallic SWNTs is much smaller than that in semiconducting SWNTs[17, 24], the energy difference for different exciton levels is much smaller in 2nm diameter metallic SWNTs. Therefore, the K-point phonon-assisted E symmetry exciton emission should appear at slightly less than 0.16eV lower energy than the bright exciton emission[23] and the Γ-point phonon-assisted emission should appear at slightly less than 0.20eV lower energy of bright exciton emission. Therefore, the side band observed in our EL measurement is more likely to be the Γ-point phonon-assisted emission. The smaller observed energy difference (0.17 eV) relative to 0.2 eV is attributed to the kinetic energy of excitons.

Figure 4 depicts the processes of the M_{11} emission (a→b) and the phonon-assisted emission (c→d→b). The intensity of the phonon-assisted emission is related to the number of excitons distributed above the M_{11} band edge with non-zero momentum and the efficiency for these excitons to emit via the phonon-assisted process. For the on-substrate sections, there may be more higher-energy excitons with non-zero momentum because a higher electric field was used in the EL measurements of the on-substrate sections, and this higher electric field will accelerate the carriers more and may create more excitons with higher energy and non-zero momentum[21]. Meanwhile, the suspended metallic SWNTs may have very low phonon-assisted emission efficiency judging from PL studies of semiconducting SWNTs. Up to now there has been no report on phonon-assisted PL from suspended semiconducting SWNTs. But phonon-assisted PL emission has been reported from surfactant-wrapped or DNA-wrapped semiconducting SWNTs[25, 26]. It is possible that due to their symmetric and unperturbed surrounding suspended semiconducting SWNTs have a low phonon-assisted efficiency. This may be the same case for our suspended metallic SWNTs, which will account for the absence of phonon-assisted EL emission.

The phonon-assisted emission energy $E_{P\text{-}A}$ can be expressed as $M_{11} + \Delta E - E_{ph}$, where ΔE is the average exciton energy relative to the zero-momentum exciton at the M_{11} edge and E_{ph} is the phonon energy. Due to the non-zero value of ΔE, the energy difference between $E_{P\text{-}A}$ and M_{11} should be less than E_{ph}, which is consistent with the experimental data. At a lower V_{ds}, ΔE is expected to be smaller since in this case there are fewer high-energy excitons in the system. Therefore the energy difference between $E_{P\text{-}A}$ and M_{11} is expected to be larger at lower V_{ds}. This is confirmed by our observations (Figure 5). At V_{ds} = 5.0 V, the energy difference between the $E_{P\text{-}A}$ and the M_{11} emission is 0.19 eV. When V_{ds} is changed to 5.6 V, it can be seen that the M_{11} emission has a red shift of 20 meV and the difference between the two peaks becomes 0.17 eV. The red shift of the M_{11} emission could be due to the increase of the lattice temperature at higher V_{ds}.[20]

The energy difference between the M_{11} emissions from the suspended and the on-substrate section as shown in Figure 2b can be attributed to environmental effects (differences in the dielectric constant of the SWNT surroundings, substrate interaction, etc.), dark-bright exciton mixing and/or the temperature difference between the suspended and the on-substrate sections under the EL experimental conditions. Because the dielectric constant of Si_3N_4 (ε = 7.5) is significantly larger than that of air (ε = 1) and the transition energy of SWNTs is smaller in higher dielectric constant surroundings[7, 27], substrates can induce a red shift of M_{11}. Van der Waals interactions with the substrates can induce an elastic deformation in the SWNTs[28] and make their transition energies shift (tens of meV)[29]. The asymmetric surrounding and higher electric field required for the emission can introduce a perturbation to the on-substrate sections. Such perturbations can promote dark-bright exciton mixing and also can induce a red shift of the transition energy (by several meV)[30, 31]. The temperatures for the suspended and on-substrate sections are unknown and the temperature difference may contribute up to a -10 meV shift in the M_{11} transition per 100-K temperature difference[32].

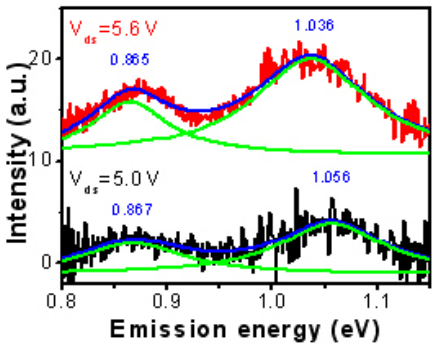

Figure 5. EL from the on-substrate section of the SWNT used in Figure 2 at different drain voltages. Red line for V_{ds} = 5.6 V, black line for V_{ds} =5.0 V. (For both data sets V_{gs} is at -20 V.) Blue lines are a Lorentzian fit to the emissions and green lines are fit curves for the individual peaks.

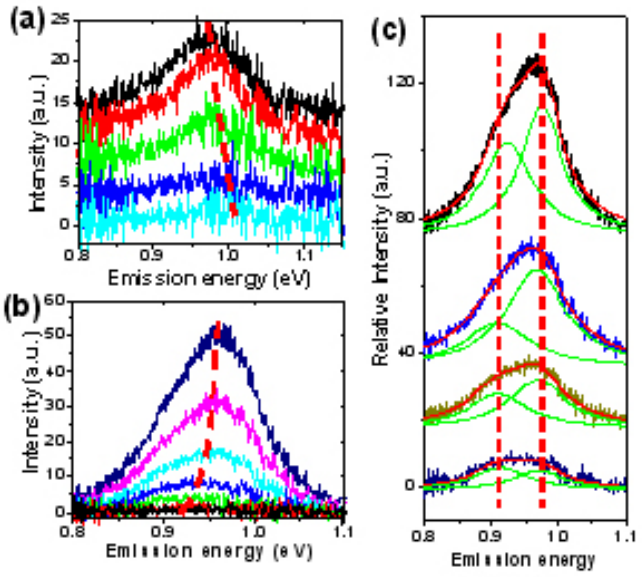

Figure 6. Red shift (a) and blue shift (b) of the EL emission position with increasing drain voltage observed for suspended sections of two different metallic SWNTs. The dashed red lines are guidance for the eyes. From bottom to top, in **(a)**, V_{ds} = 2.0-2.4 V with steps of 0.1 V, in **(b)** V_{ds} = 1.0-1.6 V with steps of 0.1 V. For all data sets V_{gs} is at -20 V. **(c)** A two-Lorentzian peak fit to the emission profiles from the suspended SWNT in (b), from bottom to up, V_{ds} = 1.3-1.6 V with a step of 0.1 V.

For the suspended sections, some SWNTs show a red shift and others show a blue shift of the EL peak standing from the V_{ds} at the onset of the EL emission and going to the V_{ds} point just before the SWNT was burnt out (Figure 6a and 6b). All EL emission from suspended sections was measured in the negative differential conductance region. Different SWNTs give different maximum energy shifts (between ±20 meV). For the suspended SWNTs, the lattice temperature of the SWNTs increases with increasing V_{ds}[11] and the transition energies (such as M_{11}) decrease with increasing temperature[32]. Therefore, in some suspended SWNTs the temperature dependence of the transition energies may dominate the EL emission shift, which gives a red shift of the EL emission with increasing V_{ds}. In other SWNTs, other factors may dominate the EL emission shift. Noticing that the EL emission peaks from the suspended section are asymmetric, the emission profile can be fit by two components: a low-energy component and a high-energy component (Figure 6c). As V_{ds} increases, the intensity of both the low-energy component and the high-energy component increase but the energy of the peak positions of these two components remain unchanged (Figure 6c). However the intensity ratio for the high-energy component to the low-energy component increases with V_{ds}, which gives rise to a blue shift of the overall spectrum. Therefore, this blue shift is due to a relatively higher intensity of the high-energy component. Since suspended SWNTs have a higher temperature at a higher V_{ds}[11], the relatively higher intensity of the high-energy component may correspond to relatively more thermally-excited excitons occupying the higher energy level. Such a higher energy level could be identified with either the M_{11} continuum and/or the M_{11}^{+} exciton level (the higher energy component of the trigonal warping-split M_{11} transition). For the SWNT shown in Figure 6c, the M_{11}^{+} exciton emission is the most likely explanation judging from the energy difference between these two emission components (~50 meV).

In conclusion, we have carried out EL measurements on suspended and on-substrate sections of the same metallic SWNTs. A phonon-assisted emission was found from the on-substrate sections, which may be due to the higher electric field and the asymmetric surroundings for the on-substrate SWNT sections. In the suspended SWNT sections, some SWNTs showed a red shift and others showed a blue shift of the EL peak position with increasing V_{ds}. The blue shift, which cannot be understood by a temperature-dependent transition energy, could be caused by the fine features of the emission spectrum at a higher

temperature, either emission from the M_{11} continuum and/or from the upper component M_{11}^{+} of the trigonal warping-split transition energies.

REFERENCES

[1] Chen, J.; Perebeinos, V.; Freitag, M.; Tsang, J.; Fu, Q.; Liu, J.; Avouris, P. *Science* **2005,** 310, (5751), 1171-1174.
[2] Lefebvre, J.; Homma, Y.; Finnie, P. *Phys. Rev. Lett.* **2003,** 90, (21), 217401.
[3] Marty, L.; Adam, E.; Albert, L.; Doyon, R.; Menard, D.; Martel, R. *Phys. Rev. Lett.* **2006,** 96, (13), 136803.
[4] Misewich, J. A.; Martel, R.; Avouris, P.; Tsang, J. C.; Heinze, S.; Tersoff, J. *Science* **2003,** 300, (5620), 783-786.
[5] O'Connell, M. J.; Bachilo, S. M.; Huffman, C. B.; Moore, V. C.; Strano, M. S.; Haroz, E. H.; Rialon, K. L.; Boul, P. J.; Noon, W. H.; Kittrell, C.; Ma, J. P.; Hauge, R. H.; Weisman, R. B.; Smalley, R. E. *Science* **2002,** 297, (5581), 593-596.
[6] Xie, L. M.; Liu, C.; Zhang, J.; Zhang, Y. Y.; Jiao, L. Y.; Jiang, L.; Dai, L.; Liu, Z. F. *J. Am. Chem. Soc.* **2007,** 129, (41), 12382-12383.
[7] Walsh, A. G.; Vamivakas, A. N.; Yin, Y.; Cronin, S. B.; Unlu, M. S.; Goldberg, B. B.; Swan, A. K. *Nano Lett.* **2007,** 7, (6), 1485-1488.
[8] Pop, E.; Mann, D.; Cao, J.; Wang, Q.; Goodson, K.; Dai, H. J. *Phys. Rev. Lett.* **2005,** 95, (15), 155505.
[9] Yao, Z.; Kane, C. L.; Dekker, C. *Phys. Rev. Lett.* **2000,** 84, (13), 2941-2944.
[10] Lefebvre, J.; Austing, D. G.; Bond, J.; Finnie, P. *Nano Lett.* **2006,** 6, (8), 1603-1608.
[11] Mann, D.; Kato, Y. K.; Kinkhabwala, A.; Pop, E.; Cao, J.; Wang, X. R.; Zhang, L.; Wang, Q.; Guo, J.; Dai, H. J. *Nat. Nanotechnol.* **2007,** 2, (1), 33-38.
[12] Jiao, L.; Fan, B.; Xian, X.; Wu, Z.; Zhang, J.; Liu, Z. *J. Am. Chem. Soc.* **2008,** 130, (38), 12612-12613.
[13] Zheng, L. X.; O'Connell, M. J.; Doorn, S. K.; Liao, X. Z.; Zhao, Y. H.; Akhadov, E. A.; Hoffbauer, M. A.; Roop, B. J.; Jia, Q. X.; Dye, R. C.; Peterson, D. E.; Huang, S. M.; Liu, J.; Zhu, Y. T. *Nat. Mater.* **2004,** 3, (10), 673-676.
[14] Collins, P. C.; Arnold, M. S.; Avouris, P. *Science* **2001,** 292, (5517), 706-709.
[15] Javey, A.; Guo, J.; Paulsson, M.; Wang, Q.; Mann, D.; Lundstrom, M.; Dai, H. J. *Phys. Rev. Lett.* **2004,** 92, (10), 106804.
[16] Strano, M. S. *J. Am. Chem. Soc.* **2003,** 125, (51), 16148-16153.
[17] Deslippe, J.; Spataru, C. D.; Prendergast, D.; Louie, S. G. *Nano Lett.* **2007,** 7, (6), 1626-1630.
[18] Saito, R.; Dresselhaus, G.; Dresselhaus, M. S. *Phys. Rev. B* **2000,** 61, (4), 2981-2990.
[19] Wang, X.; Zhang, L.; Lu, Y.; Dai, H.; Kato, Y. K.; Pop, E. *Appl. Phys. Lett.* **2007,** 91, (26), 261102.
[20] Pop, E.; Mann, D. A.; Goodson, K. E.; Dai, H. J. *J. Appl. Phys.* **2007,** 101, (9), 093710.
[21] Perebeinos, V.; Avouris, P. *Phys. Rev. B* **2006,** 74, (12), 121410.
[22] Srivastava, A.; Htoon, H.; Klimov, V. I.; Kono, J. *Phys. Rev. Lett.* **2008,** 101, (8), 087402.
[23] Torrens, O. N.; Zheng, M.; Kikkawa, J. M. *Phys. Rev. Lett.* **2008,** 101, (15), 157401.
[24] Wang, F.; Dukovic, G.; Brus, L. E.; Heinz, T. F. *Science* **2005,** 308, (5723), 838-841.
[25] Lebedkin, S.; Hennrich, F.; Kiowski, O.; Kappes, M. M. *Phys. Rev. B* **2008,** 77, (16), 165429.
[26] Chou, S. G.; Plentz, F.; Jiang, J.; Saito, R.; Nezich, D.; Ribeiro, H. B.; Jorio, A.; Pimenta, M. A.; Samsonidze, G. G.; Santos, A. P.; Zheng, M.; Onoa, G. B.; Semke, E. D.; Dresselhaus, G.; Dresselhaus, M. S. *Phys. Rev. Lett.* **2005,** 94, (12), 127402.
[27] Miyauchi, Y.; Saito, R.; Sato, K.; Ohno, Y.; Iwasaki, S.; Mizutani, T.; Jiang, J.; Maruyama, S. *Chem. Phys. Lett.* **2007,** 442, (4-6), 394-399.
[28] Hertel, T.; Walkup, R. E.; Avouris, P. *Phys. Rev. B* **1998,** 58, (20), 13870-13873.
[29] Shan, B.; Lakatos, G. W.; Peng, S.; Cho, K. J. *Appl. Phys. Lett.* **2005,** 87, (17), 173109.
[30] Shaver, J.; Kono, J.; Portugall, O.; Krstic, V.; Rikken, G. L. J. A.; Miyauchi, Y.; Maruyama, S.; Perebeinos, V. *Nano Lett.* **2007,** 7, (7), 1851-1855.
[31] Mortimer, I. B.; Nicholas, R. J. *Phys. Rev. Lett.* **2007,** 98, (2), 027404.
[32] Cronin, S. B.; Yin, Y.; Walsh, A.; Capaz, R. B.; Stolyarov, A.; Tangney, P.; Cohen, M. L.; Louie, S. G.; Swan, A. K.; Unlu, M. S.; Goldberg, B. B.; Tinkham, M. *Phys. Rev. Lett.* **2006,** 96, (12), 127403.

4. Direct Deposition of Single-walled carbon nanotubes thin films via Electrostatic spray-assisted chemical vapor deposition

Sponsors
Partial funding by the Materials, Structure and Device center, one of the five centers in the Focus Center Research Program (FCRP). Y.P H. acknowledges financial support from the National Science Council of the Republic of China through Project No. 096-2917-I-002-005.

Project Staff
Ya-Ping Hsieh, Mario Hofmann, Hyungbin Son, Xiaoting Jia, Yang-Fang Chen, Chi-Te Liang, Mildred S. Dresselhaus, and Jing Kong

1. Introduction

Single-walled carbon nanotube (SWNT)-based monolayer- or submonolayer-thin films on substrates represent a material platform that is attractive for many applications, such as thin film transistors for display and flexible electronics, transparent electrodes [1-6], substrates for neuron cell growth and stimulation [7], etc. In order to obtain such a thin film of SWNTs on substrates, most approaches are solution-based, i.e., a bulk amount of SWNT material is purified and dispersed in solution, and is deposited on the substrate afterwards via different techniques, such as drop casting, spraying [5, 6] or vacuum filtration [4]. The purification and dispersion steps are costly and time consuming. More importantly, due to the sonication treatment during these steps, defects are created along the length of SWNTs, and the nanotubes are cut to an average length of 1 μm or less. As a result, the electrical properties of these SWNTs films are degraded. Here we use a floating catalyst chemical vapor deposition (CVD) method to directly coat a substrate with SWNT thin films. The catalyst is dispersed into an aerosol produced by electro-spraying since this method [8, 9] is expected to provide small, highly charged droplets with a narrow diameter distribution when using a strong applied electrical field [10]. These droplets of ethanol solution containing ferrocene provide both the catalyst and carbon precursor for the SWNT growth. Once the nanotubes are generated in the hot zone, they are carried by the gas flow and deposit on a low temperature surface at the downstream end of the furnace. Atomic force microscopy (AFM) and Raman spectroscopy are used as characterization techniques to examine where the nanotubes deposit inside the furnace. It was found that the SWNTs are mainly deposited at specific locations, instead of uniformly coating the inside of the reactor. By considering different types of forces acting on the floating SWNTs, the preferential SWNT deposition at specific locations can be understood. By optimizing the CVD process parameters, films consisting mostly isolated SWNTs could be obtained, as confirmed by comparison of Raman and AFM size distributions. Furthermore, an investigation of the length distributions of nanotubes deposited at different locations indicates the potential of in-situ SWNT sorting.

2. Experimental

Figure 1 is a schematic depiction of our synthesis setup: Ethanol (99.9 %, Aldrich) with 0.01 M Ferrocene (99 %, Aldrich, 1.86 mg/ml) is used as the catalyst and carbonaceous precursor, respectively, and is introduced into a spray nozzle. The solution is dispersed into an aerosol when the surface tension of the liquid/air interface is overcome by a strong electrostatic field (on the order of 10^6 V/m) applied between the spray nozzle (-6 kV) and the counter electrode (Ground) (as indicated in the inset of Fig. 1). Subsequently small droplets are extracted from the spray nozzle. The precursor solution was delivered to the spray nozzle at a flow rate of 8 ml/hr. The atomized and charged droplets of the precursor solution are carried into the growth chamber by a flow of argon/hydrogen (with a volume ratio of 61/39 and a total flow rate of 1000 sccm). Silicon substrates with 100nm thermally grown oxide (SiO_2/Si) were placed inside the chamber to collect the grown nanotubes (Fig. 1). In order to investigate the deposition of SWNTs throughout the furnace, long SiO_2/Si substrates were stacked to cover the entire length of the furnace (35 cm). Three growth temperatures, 950°C, 1000°C and 1100°C, were used in this study. The growth time was usually 4 minutes, after which the catalyst delivery was turned off and the samples were cooled down under Ar/H_2 flow. After the CVD process, AFM imaging and confocal Raman mapping across the surface of the substrates were used to characterize the SWNT deposition. The temperature inside the furnace and substrate temperatures at different locations were measured using two K-type thermocouples that reached into the reaction zone.

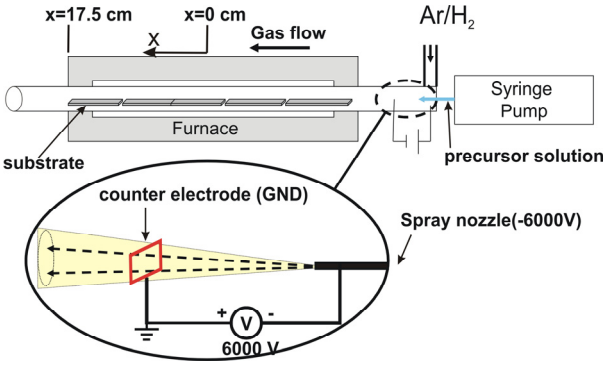

Figure 1: A schematic diagram of the synthesis setup: x is the position along the CVD chamber, and x=0 is designated to be the furnace center. The edge of the furnace at the downstream end is x=17.5cm. Inset: close up of the spray nozzle with an indication of the electrical field.

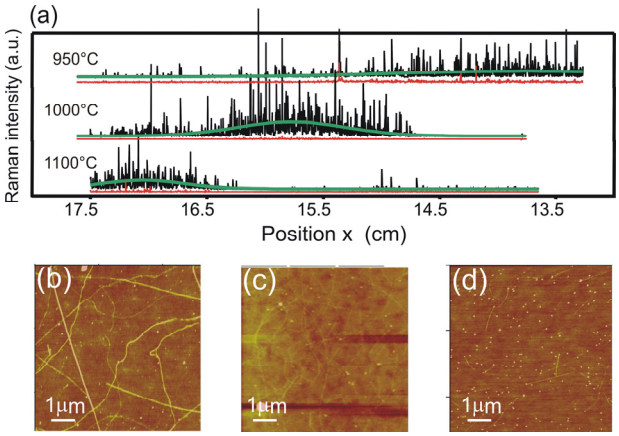

Figure 2: (a) Spatial distribution of the integrated G band intensity (1500 cm^{-1}~1650 cm^{-1}) (black), the integrated D-band intensity (1250cm^{-1}~1400cm^{-1}) (red) and the fitted G-band intensity (green) for three different growth temperatures: 950, 1000 and 1100°C. (b-d) Representative AFM images of the sample morphology taken at the center of the density distributions for 950°C **(b)**, 1000°C **(c)**, and 1100°C **(d)** growth temperatures.

3. Results and discussion

In order to characterize the materials deposited on the substrates, confocal Raman spectroscopy (with a laser spot of ~1 μm^2) was used to scan a line across the substrates, with a step size of 35 μm using an excitation wavelength of 532nm. The G-band, a Raman mode at around 1600 cm^{-1} and associated with the in-plane vibrations of sp^2 carbonaceous species was used to examine the deposition of the obtained material. The intensity variation of this Raman feature across the sample can give an overview of the spatial distribution of the nanotube density [11]. Figure 2(a) presents the integrated G band intensity (1500cm^{-1}~1650cm^{-1}) vs position x (black) for three different growth temperatures. It can be seen that most carbonaceous materials are deposited in the region close to the edge of the heating zone (x=17.5 cm, Fig. 1) at the downstream end of the furnace. In other locations, almost no G band intensity was observed.

The integrated intensity of the Raman D band around 1300 cm^{-1} (from 1250 cm^{-1} to 1400 cm^{-1}) vs position x for these three growth temperatures are also shown in Fig 2(a) underneath the corresponding G-band distribution. The D band in the Raman spectrum is known to arise from the defects in sp^2 structures. The average ratio of our G/D band intensities is about 50. This low D band intensity indicates that our samples contain high quality graphitic structures and a low content of amorphous carbon material. This is consistent with Figure 2(b)-(d) where AFM images were taken at the center of the density distributions for 950°C (b), *1000°C (*c), and 1100°C (d) growth temperatures and they show that most of the deposited materials are SWNTs. The average spatial distribution of the G-band intensities (green curves in Fig 2(a)) follows a Gaussian distribution and its center shifts toward the downstream edge as the growth temperature increases. On the other hand, the width of the fitted Gaussian distribution becomes larger at lower growth temperatures. From the G band intensity distribution in Fig. 2(a) it can be seen that in order to obtain a uniform coating on the substrate, the sample size would have to be limited to 2 cm for the 1000°C case, whereas for the 950°C growth, there is a wider range (>3 cm) for an even coat of SWNTs on the substrate.

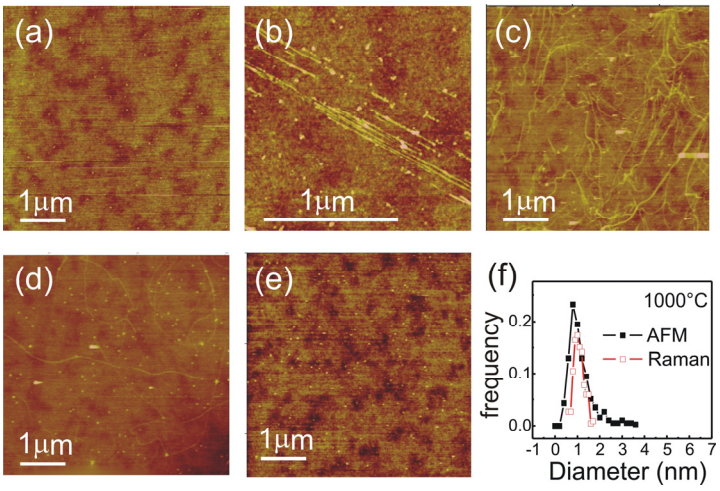

Figure 3: (a) Representative AFM images of the growth results at different positions x along the furnace: **(a)** 14 cm **(b)** 14.5 cm **(c)** 15.5 cm **(d)** 16.5 cm **(e)** 17.5 cm (growth temperature 1000°C) (d) Diameter distribution of the SWNTs around position (d) as obtained by Raman and AFM measurements taken from 435 and 450 nanotubes, respectively.

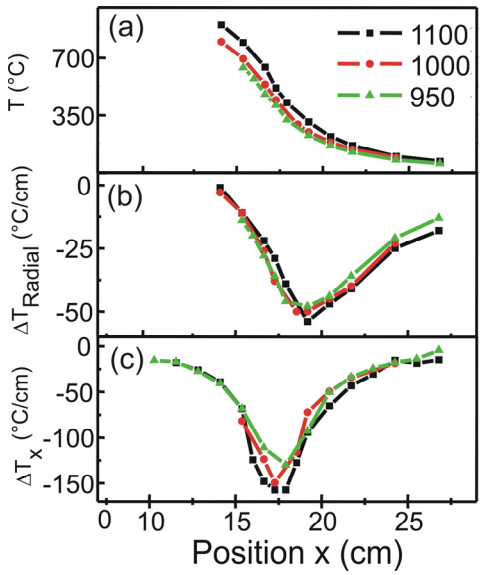

Figure 4: (a) Spatial temperature distribution along the x direction. Spatial temperature gradient distribution **(b)** in the radial and **(c)** x directions.

Figure 3 presents a series of AFM images taken on substrates at different locations inside the furnace for the growth temperature of 1000°C. The density of SWNTs in Fig 3(a)-(e) is consistent with the measurement of variation of the average integrated G band intensity in Fig. 2(a).

The diameter distribution of the nanotubes is derived independently from analysis of AFM images from 450 nanotubes and their Raman characterization (Fig. 3(f)). Confocal Raman spectra with eight different laser excitation wavelengths (457 nm, 488 nm, 514 nm, 532 nm, 594 nm, 647 nm, 675 nm, 780 nm) were taken in a 200 μm × 40 μm area in the same spatial region as the AFM images were taken to ensure a representative coverage of nanotubes with different resonance condition. The diameter of each individual nanotube was determined from the frequency of its RBM mode [12, 13] using formula A=218.8/B -15.9 where A and B are the frequency of the RBM mode and the diameter, respectively Good agreement between the two diameter distributions derived by AFM and Raman measurements(Fig 3(f)) is observed. This indicates the absence of a significant amount of nanotube bundles because the diameter derived from the AFM height measurement - representing the diameter of the entire bundle- would differ from the distribution from Raman analysis which only probes the diameters of individual SWNTs within this bundle. Thus it can be seen that for the growth at 1000°C most deposited nanotubes are isolated SWNTs, which is very important for certain applications [14, 15]. We attribute this high probability of depositing isolated SWNTs to the fact that we used a much more dilute concentration of both the ferrocene catalyst and the carbon precursor (compared with ref. [16], the carbon precursor is about 16 times more dilute in the carrier gas and the ferrocene to carbon precursor ratio is about 10 times less.) as well as the small diameter of the generated aerosol particles that is expected from electro-spray dispersion. As a result, the as-grown SWNT aerosol concentration inside the furnace is much reduced and the nanotubes have less chance to interact with each other in the gas phase to form bundles. Furthermore it is worth mentioning that the diameter distribution is fairly narrow, ~±0.3 nm, and the average diameter is <1 nm, which makes these nanotubes very useful for optical and spectroscopic applications [17, 18].

In order to understand the distribution of SWNT density as a function of their position on the substrate, thermocouple temperature measurements were conducted across the cross section of the reaction chamber (termed radial direction as the chamber is cylindrical) and along the length of the reaction chamber (termed x-direction in Fig. 1). Figure 4 displays the gas-temperature (Fig 4(a)) and the temperature gradients ΔT in the radial (Fig 4(b)) and x-direction (Fig 4(c)) as a function of position x along the chamber. The radial temperature gradient is approximated by taking the difference of the gas and the substrate temperature at the same x. It is expected that the walls (which are subjected to a more intimate heat transfer from the furnace and the environment) are cooling down faster than the gas stream, and

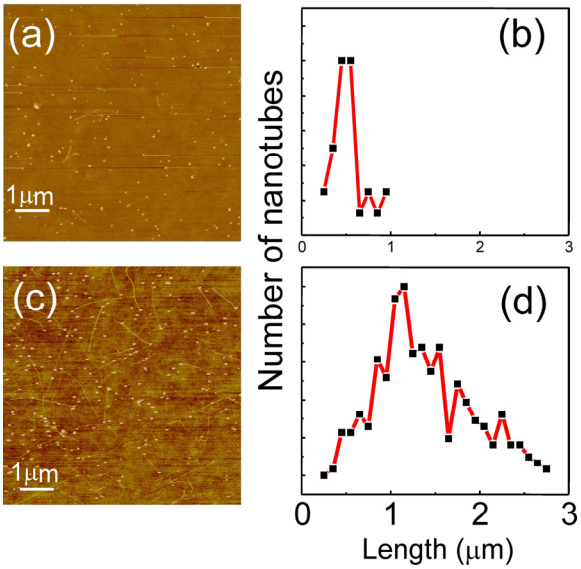

Figure 5: AFM images of SWNTs grown at 1100°C and collected at x=16.2cm (a) and 17.4cm (c) respectively. Length distributions for the obtained nanotubes at x=16.2cm (b) and 17.4cm (d). Growth temperature was 1100°C.

indeed it can be seen in Fig 4(c) that ΔT in the radial direction increases in magnitude towards the downstream edge of the furnace. This temperature gradient will give rise to a thermophoretic force on the floating SWNTs in the radial direction [19], driving them towards the colder substrate and depositing them on the substrate. In addition, the floating aerosol particles (including SWNTs) in the gas stream experience other types of driving forces that will move them in the x-direction: (1) Diffusion because of a density gradient of the produced SWNTs along the furnace will direct them from the reaction zone, where they are grown, towards the two ends of the furnace tube; (2) A thermophoretic force in the x-direction due to the changes in temperature along the x direction as shown in Fig 4(a) will give rise to a motion of the particle away from the hot reaction zone; (3) The gas flow will exert a drag force on the particle towards the downstream direction. This drag force is strongly dependent on the size of the particles, especially if they become comparable to the mean free path of the gas molecules [20]. From Fig. 3(b) we can see that as we follow the gas flow direction from upstream to downstream, the materials which precipitated on the substrate first consists of very short, broken pieces of SWNTs. We attribute this to the fact that since these pieces are short, the drag force on them due to the gas flow is small. At the same time the small mass of these particles gives them larger mobility in small temperature gradients, which appear closer to the reaction zone. As a result these fragments start to precipitate at a location earlier than larger nanotubes.

Longer nanotubes, on the other hand experience (apart from the diffusion and thermophoretic forces) a stronger drag force and are carried further downstream and deposit at a later position. This implies that the floating catalyst CVD can be potentially used for in-situ separation of SWNTs if varying forces can be applied to different types of SWNTs. Thus it is possible for SWNTs of different lengths to be spatially separated. Indeed, the results in Fig. 5 confirm this point. Figure 5 (a) and (c) are AFM images of SWNTs grown at 1100°C and collected at 16.2 cm and 17.4 cm respectively (Growth conditions correspond to the ones used in Fig. 2(a)). A high ethanol decomposition rate at this temperature results in carbon coating over the catalyst (as indicated by the increased size of catalyst clusters in Fig. 5(a) and (c)) and therefore the catalyst lifetime becomes shorter. As a result, the SWNTs are much shorter compared to the 950 and 1000 °C cases. These short SWNTs simplify the observation of the length dependent separation by AFM. Figures 5(b) and (d) show the length distributions of the SWNTs collected at the same positions (28 SWNTs and 288 SWNTs are used for the distributions, respectively). It can be seen that SWNTs with an average length <1 um precipitate earlier than SWNTs with average length >1 μm.

Our analysis of the various forces acting on the floating aerosol particles (SWNTs and catalyst particles, etc) helps to explain other experimental observations as well. For example, if the growth conditions are not tuned well (i.e. when using too high concentrations of carbon precursor), amorphous carbon will deposit even at the upstream edge of the furnace (region -16.5cm ~ -17.5cm). This can be understood if one considers the following scenario: The floating amorphous carbon particles are too small to experience a significant drag force from the gas flow. Since there are diffusive and thermophoretic forces in both directions along the chamber they can drive the particles from the hot zone to both ends of the furnace. As a result, some of the particles are moving against the flow and are finally deposit at the upstream cold region.

Finally we note that the comparison of the SWNT spatial distributions of the three growth temperatures provides further insights into the growth of the SWNTs. As shown in Fig. 2(a), the center of the average spatial distribution shifts toward the downstream edge as the growth temperature increases. On the other hand, Fig. 4(b) and 4(c) show that both the axial and the radial temperature gradients are very similar in

the regions of interest for the three growth temperatures (Fig. 4(a)) and cannot explain the observed trends. However, the diffusion of nanotubes away from the reaction zone is expected to increase with increasing temperature and indeed we see that nanotubes grown at 1100°C deposit further downstream than the ones grown at 1000°C or 950°C. This result also sheds some light on the lesser importance of drag force compared to diffusivity: Since the average length of the nanotubes grown at 950°C is much higher than the nanotubes grown at 1100°C, the drag force would cause the opposite trend. Instead the temperature and inverse length dependences of the diffusivity [21] prevail and cause the observed tendency in the center position of the density distribution.

4. Conclusions

In this work, we used floating catalyst CVD to directly deposit very thin films of SWNTs on substrates, which is important for many applications. If a low nanotube concentration condition (i.e., low catalyst concentration and low ethanol injecting rate) is maintained, an isolated nanotube film can be obtained. The deposition of floating SWNTs on the substrate can be explained by analyzing the forces acting on them. A length separation of nanotubes deposited at different positions was observed which shows potential for future applications.

References

[1] Snow E S, Campbell P M, and Ancona M G, Novak J P 2005 *Appl. Phys.Lett.* **86**, 033105.
[2] Takenobua T, Takahashi T, Kanbara T, Kazuhito Tsukagoshi; Aoyagi Y and Iwasa Y 2006 *Appl. Phys.Lett.* **88**, 033511.
[3] Zhang M, Fang S,1 Zakhidov A A, Lee S B, Aliev A E, Williams C D, Atkinson K R and Baughman R H. 2006 *Science* **309** 1215.
[4] Wu Z, Chen Z, Du X, Logan J M, Sippel J, Nikolou M, Kamaras K, Reynolds J R, Tanner D B, Hebard A F and Rinzler A G. 2004 *Science* **305** 1273.
[5] Duggal R, Hussain F and Pasquali M 2006 *Adv. Mater.* **18** 29.
[6] Li Y, Kinloch I A and Windle A H 2004 *Science* **304** 276.
[7]Mazzatenta A, Giugliano M, Campidelli S, Gambazzi L, Businaro L, Markram H, Prato M and Ballerini L 2007 *J. Neurosci.* **27(26)** 6931.
[8] Wei M, Zhi D and Choy K 2006 *Nanotechnology* **17** 181.
[9] Li W Z, Wen J G and Ren Z F 2002 *Appl. Phys. A* **74** 397.
[10] Chen D, Pui D Y H and Kaufmar S L 1995 *J. Aerosol Sci*. **26** 963.
[11] Hart A J, Slocum A H and Royer L 2006 *Carbon* **44** 348.
[12] Araujo P T, Doorn S K, Kilina S, Tretiak S, Einarsson E, Maruyama S, Chacham H, Pimenta M A and Jorio A 2007 *Phys. Rev. Lett.* **98**, 067401.
[13] Rao A M, Richter E, Bandow S, Chase B, Eklund P C, Williams K A, Fang S, Subbaswamy K R, Menon M, Thess A, Smalley R E, Dresselhaus G and Dresselhaus M S 1997 *Science* **275** 187.
[14] Furtado C A, Kim U J, Gutierrez H R, Pan L, Dickey E C and Eklund P C 2004 *J. Am. Chem. Soc.*, **126 (19)** 6095.
[15] Wang H, Zhou W, Ho D L, Winey K I, Fischer J E, Glinka C J and Hobbie E K 2004 *Nano Lett.* **4** 1789.
[16] Zhu H W, Xu C L, Wu D H, Wei B Q, Vajtai R and Ajayan P M 2002 *Science* **296** 884.
[17] Yamashita S, Inoue Y, Maruyama S, Murakami Y, Yaguchi H, Jablonski M and Set S Y 2004 *Opt. Lett.* **29** 1581.
[18] Schibli T R, Minoshima K, Kataura H, Itoga E, Minami N, Kazaoui S, Miyashita K, Tokumoto M and Sakakibara Y 2005 *Opt. Expres* **13** 8025.
[19] Batchelor G K and Shen C 1985 *J. Colloid Interface Sci*. **107** 21.
[20] Matthews M T and Hill J M 2006 *Quart. J. Mech. Appl. Math.* **59** 191.
[21] Tirado M M, Martinez C L and Delatorre J G 1984 *J. Chem. Phys.* **81** 2047.